Black hole-neutron star mergers with massive neutron stars in numerical relativity

Shichuan Chen,[1,2,3] Luohan Wang,[4,3] Kota Hayashi,[3,5] Kyohei Kawaguchi,[3,5,6] Kenta Kiuchi,[3,5] and Masaru Shibata[3,5]

[1]*Department of Astronomy, School of Physics, Peking University, Beijing 100871, China*
[2]*Kavli Institute for Astronomy and Astrophysics, Peking University, Beijing 100871, China*
[3]*Max Planck Institute for Gravitational Physics (Albert Einstein Institute), Am Mühlenberg 1, Postdam-Golm 14476, Germany*
[4]*School of Physics, Peking University, Beijing 100871, China*
[5]*Center for Gravitational Physics and Quantum Information, Yukawa Institute for Theoretical Physics, Kyoto University, Kyoto 606-8502, Japan*
[6]*Institute for Cosmic Ray Research, The University of Tokyo, 5-1-5 Kashiwanoha, Kashiwa, Chiba 277-8582, Japan*

(Received 29 April 2024; accepted 30 July 2024; published 10 September 2024)

We study the merger of black hole-neutron star (BH-NS) binaries in numerical relativity, focusing on the properties of the remnant disk and the ejecta, varying the mass of compactness of the NS and the mass and spin of the BH. We find that within the precision of our numerical simulations, the remnant disk mass and ejecta mass normalized by the NS baryon mass ($\hat{M}_{\rm rem}$ and $\hat{M}_{\rm eje}$, respectively), and the cutoff frequency $f_{\rm cut}$ normalized by the initial total gravitational mass of the system at infinite separation approximately agree among the models with the same NS compactness $C_{\rm NS} = M_{\rm NS}/R_{\rm NS}$, mass ratio $Q = M_{\rm BH}/M_{\rm NS}$, and dimensionless BH spin $\chi_{\rm BH}$ irrespective of the NS mass $M_{\rm NS}$ in the range of $1.092 - 1.691 M_\odot$. This result shows that the merger outcome depends sensitively on Q, $\chi_{\rm BH}$, and $C_{\rm NS}$ but only weakly on $M_{\rm NS}$. This justifies the approach of studying the dependence of NS tidal disruptions on the NS compactness by fixing the NS mass but changing the EOS. We further perform simulations with massive NSs of $M_{\rm NS} = 1.8 M_\odot$, and compare our results of $\hat{M}_{\rm rem}$ and $\hat{M}_{\rm eje}$ with those given by existing fitting formulas to test their robustness for more compact NSs. We find that the fitting formulas obtained in the previous studies are accurate within the numerical errors assumed, while our results also suggest that further improvement is possible by systematically performing more precise numerical simulations.

DOI: 10.1103/PhysRevD.110.063016

I. INTRODUCTION

The first gravitational wave (GW) detection for GW150914 from a binary black hole (BBH) merger heralded the opening of the era of GW astronomy [1]. Subsequently, at the event of GW170817, the first binary neutron star (BNS) merger was observed not only through GWs but also through signals of electromagnetic (EM) counterparts by diverse instruments all over the world [2–6]. GW data analysis for this event gave a constraint on the tidal deformability of the NS which excludes very stiff equations of state (EOS) [2,7–10]. The observation of short gamma-ray burst (GRB), GRB 170817A, and the kilonova, AT2017gfo, indicated that the NS is involved in the merger, and it is suggested that a remnant formed after a BNS merger is likely to be the central engine of the GRB [4,5,11]. The observation of the kilonova indicated that an *r*-process nucleosynthesis could occur in the BNS merger. All these facts suggest that future observations of GWs and EM counterparts will provide us valuable opportunities to deepen the knowledge of the mechanism of short GRBs, kilonovae, and *r*-process nucleosyntheses of heavy elements.

As in the BNS mergers, the BH-NS mergers can also, in principle, generate EM counterparts of GW such as kilonovae when a significant amount of matter is ejected in the tidal disruption of the NS. Such EM counterparts can give information about the NS EOS [8,12], the origin of heavy elements produced through *r*-process nucleosynthesis [13–17], and cast light on physics beyond the nuclear saturation density. However, although two events GW200105 and GW200115 [18] are reported to be the BH-NS merger in 2021, and in addition, GW190425 (with masses of

$1.12-1.68M_\odot$ and $1.61-2.52M_\odot$) could possibly be a BH-NS merger [19,20], no multimessenger detection of BH-NS mergers has been confirmed yet. This lack of EM counterpart observation for the previous events is consistent with theoretical predictions because the mass ratios of these binaries are as high as 4–5 and the BH spins are likely to be zero or retrograde, and thus, tidal disruption is unlikely to occur [21]. However, for interpreting future events, in which tidal disruption of NSs may occur, it is crucial to prepare theoretical models that quantify the relation between the properties of the BH-NS merger and the observables.

Numerical simulations of BH-NS mergers play an important role in understanding the tidal disruption and mass ejection processes. Since 2006 [22–26], many numerical simulations have been performed for this to study the dependence of the merger behavior on binary parameters, focusing on the characteristic results of tidal disruptions [27–43]. Additionally, it is revealed that the cutoff frequency, one of the notable features of the GW signal in tidal disruptions, encodes information on the NS EOS, especially when it is stiff [29,31,44,45]. More importantly, previous studies [32,33,38,46,47] show that the rest mass of the remnant matter located outside the apparent horizon and ejecta mass normalized by the NS baryon mass ($\hat{M}_{\rm rem}$ and $\hat{M}_{\rm eje}$, respectively) as well as the cutoff frequency of GWs depend sensitively only on the mass ratio Q, the BH dimensionless spin $\chi_{\rm BH}$, the compactness of NSs $C_{\rm NS}$ but not on the NS mass $M_{\rm NS}$. Based on this approximate parameter dependence, previous studies [33,38,46,47] of BH-NS mergers give some fitting formulas for the remnant mass $M_{\rm rem}$ and the ejecta mass $M_{\rm eje}$. These semi-analytical models for the merger results are valuable because numerical simulations of BH-NS mergers are resource-intensive. These fitting formulas for the remnant disk mass and ejecta mass are used to assess whether the EM counterparts would be present [38,48], and constrain the binary parameters after the observation of EM signals [49–54].

However, the typical range of NS mass in these previous simulations is limited to $M_{\rm NS}\approx 1.2$–$1.5M_\odot$ [55,56], with NS compactness between 0.12 and 0.19, although more massive NSs at least up to $\sim 2M_\odot$ exist in nature [57,58]. It is not clear whether the fitting formulas obtained by the previous studies also hold quantitatively for more massive and compact NSs because they are not tested for more massive NSs. Given possible GW detections of such massive NSs in BH-NS binaries [19,59], quantitative investigation of the BH-NS mergers in such a parameter space is essential.

In this paper, we study BH-NS mergers in numerical relativity varying the NS mass and NS compactness for a range wider than in the previous studies. We first focus on BH-NS binaries with the several fixed combinations of mass ratio Q, BH dimensionless spin $\chi_{\rm BH}$, and NS compactness $C_{\rm NS}$ but with various NS masses $M_{\rm NS}$ in order to clarify how $\hat{M}_{\rm rem}$, $\hat{M}_{\rm eje}$, and $f_{\rm cut}m_0$ (where $m_0=M_{\rm BH}+M_{\rm NS}$) are sensitive to the NS mass $M_{\rm NS}$. We then perform simulations for a large value of the NS mass ($M_{\rm NS}=1.8M_\odot$), and examine the accuracy of the previous fitting formulas of $\hat{M}_{\rm rem}$, $\hat{M}_{\rm eje}$, and ejecta velocity $v_{\rm eje}$ for the system with a large value of the NS compactness ($C_{\rm NS}\geq 0.19$). We will show that within the range of the numerical accuracy, $\hat{M}_{\rm rem}$, $\hat{M}_{\rm eje}$, and $f_{\rm cut}m_0$ can be derived from the fitting formulas if the values of $\chi_{\rm BH}$, Q, and $C_{\rm NS}$ are identical: The fitting formulas previously obtained in Refs. [38,46,47] still work well for larger values of $C_{\rm NS}$ above 0.19.

The paper is organized as follows. In Sec. II we briefly summarize numerical methods used in our study. Numerical results of simulations are presented in Sec. III, focusing on the remnant disk mass, the ejecta mass, and the gravitational waveforms. In Secs. III B and III C, we present the results for the simulations with the fixed NS compactness and those for massive and compact NSs, respectively. Section IV is devoted to a summary and discussion. Throughout this paper, all the quantities in tables and figures are shown in units of $c=G=M_\odot=1$ unless otherwise stated. Our convention of notation is summarized in Table I.

TABLE I. Our convention of notation for physically important quantities, geometric variables, and hydrodynamic variables.

Symbol	Description
$M_{\rm BH}$	Gravitational mass of the black hole in isolation
$\chi_{\rm BH}$	Dimensionless spin parameter of the black hole
$M_{\rm NS}$	Gravitational mass of the neutron star in isolation
$R_{\rm NS}$	Circumferential radius of the neutron star in isolation
$M_{\rm b}$	Rest baryon mass of the neutron star in isolation
$C_{\rm NS}$	Compactness of the neutron star: $C_{\rm NS}=M_{\rm NS}/R_{\rm NS}$
Q	Mass ratio of BH-NS: $Q=M_{\rm BH}/M_{\rm NS}$
$M_{\rm rem}$	Remnant disk mass after the merger
$M_{\rm eje}$	Ejecta mass after the merger
$\hat{M}$	Mass normalized by $M_{\rm b}$
m_0	Initial total gravitational mass of the system at infinite separation
γ_{ij}	Induced metric on the $t=$ const hypersurface
α	Lapse function
β^i	Shift vector
γ	Determinant of γ_{ij}
ρ	Baryon rest-mass density
u^μ	Four velocity of the fluid
P	Pressure
ϵ	Specific internal energy
ρ_*	Conserved baryon rest mass density: $\rho\alpha\sqrt{\gamma}u^t$
Γ	Adiabatic index
h	Specific enthalpy: $1+\epsilon+P/\rho$
$\hat{e}$	Specific energy: $h\alpha u^t-P/\rho\alpha u^t$

II. NUMERICAL METHODS

This section describes the numerical methods used in our study. Sec. II A summarizes our numerical simulation methods, Sec. II B describes the NS EOS, Sec. II C presents the diagnostics of simulations, Sec. II D presents the fitting formulas given from previous studies, and Sec. II E presents the models employed in this study.

A. Simulation methods

We carry out numerical simulations using the SACRA-MPI code [60], which uses an adaptive-mesh-refinement (AMR) algorithm [27] and MPI / OpenMP hybrid parallelization to speed up the computation [60]. SACRA solves the Einstein equation in a moving puncture version [61–63] of the Baumgarte-Shapiro-Shibata-Nakamura (BSSN) formulation [64,65], incorporating a Z4c constraint-propagation prescription locally [66]. Together with the Einstein equation, we solve hydrodynamics equations using the Harten-Lax-van Leer contact (HLLC) solver [67–69] in this paper. More details of the formulation, the gauge conditions, and the numerical scheme are described in Refs. [31,32,42,45]. For actual computation, we employ the public spectral code FUKA (Frankfurt University Kadath) [70] to generate initial data. We do not take into account magnetohydrodynamics and neutrino-transfer effects, since we focus on the evolution of the system up to 30 ms after the merger for which these effects are not very important.

The grid structure of SACRA is summarized as follows. Computational domains are composed of nested equidistant Cartesian grids, and each grid has $(2N, 2N, N)$ points in (x, y, z) directions. We employ a cell-centered grid structure and the x-coordinate at jth grid point is given by $x_j = (j + 1/2)\Delta x$, where Δx is the grid resolution. The equatorial-plane symmetry is imposed on the $z = 0$ plane. We adopt $N = 82$ as a fiducial value, with which the NS radius is covered by ≈66 points in the finest grid. We also perform simulations with $N = 62$ and $N = 102$ for selected models to evaluate the numerical error and check the convergence of the numerical results (see Appendix A). The physical quantities in tables and figures, unless specified, are taken from results with $N = 82$. In our study, the inspiral motion before the merger is followed at least for 5 orbits.

We prepare 10 refinement levels for the AMR computational domains. 6 coarser domains (l_c) cover both BH and NS with the origins fixed at the center of the mass of the binary system. Two sets of 4 finer domains (l_f) comove with either BH or NS, covering the region of their vicinity. Namely, we prepare $2l_f + l_c$ computational grid domains spanning $l_c + l_f$ refinement levels. Starting from the coarsest level as $l = 0$, the lth level has a grid spacing, $\Delta x_l = L/(2^l N)$, and at the finest level, $\Delta x = L/(2^{l_f+l_c-1}N)$, where L is the size of the computational domain, which covers $[-L:L] \times [-L:L] \times [0:L]$ for x-y-z.

B. Equation of state

Since the lifetime of NS binaries is typically much longer than the cooling time of NSs, NSs in the late inspiral stage are believed to be cold enough to be modeled by zero-temperature EOS [71]. Thus, for modeling the NSs prior to the merger, we use the zero-temperature EOS in our simulations. In this paper, we model such EOSs by piecewise polytropes [72–74], which are written in the form

$$P(\rho) = \kappa_i \rho^{\Gamma_i} (\rho_i \le \rho \le \rho_{i+1}), \tag{1}$$

where κ_i are constants and other quantities are described in Table I. We perform simulations for models with both two pieces and four pieces, with $i \in \{0, 1\}$ and $i \in \{0, 1, 2, 3\}$ respectively. $\rho_0 = 0$, and for $\rho \le \rho_1$, we adopt $\Gamma_0 = 1.35692395$ and $\kappa_0/c^2 = 3.99873692 \times 10^{-8}\,\mathrm{g}^{1-\Gamma_0}\,\mathrm{cm}^{3\Gamma_0-3}$ [72]. The boundary condition at ρ_i is $\kappa_i \rho_i^{\Gamma_i} = \kappa_{i+1}\rho_i^{\Gamma_{i+1}}$, which requires the continuity of pressure at the interface between ith and $(i + 1)$th region.

For different EOS models, we take different fiducial pressures $P_{\rm fid}$ at the fiducial density $\rho_{\rm fid} = 10^{14.7}\ \mathrm{g\,cm^{-3}}$. For piecewise polytropes with two pieces, we take $\rho_2 \to +\infty$, $\Gamma_1 = 3.000$, and κ_1 is defined by $\kappa_1 = P_{\rm fid}/\rho_{\rm fid}^{\Gamma_1}$. For piecewise polytropes with four pieces, we take $\rho_2 = \rho_{\rm fid}$, $\rho_3 = 10^{15}\ \mathrm{g\,cm^{-3}}$, $\rho_4 \to +\infty$, and κ_2 is defined by $\kappa_2 = P_{\rm fid}/\rho_{\rm fid}^{\Gamma_2}$. Other parameters for different EOS models and NS initial properties related to the EOS are listed in Table II.

In numerical simulations, we add the thermal part of the EOS to the zero-temperature part described above. Our implementation for it is the same as that described in Refs. [75] with an adiabatic index of the thermal part $\Gamma_{\rm th} = 1.8$.

C. Diagnostics

1. Remnant disk and ejecta

After the merger, the fate of the matter originating from the NS can be divided into three types. The matter directly

TABLE II. Piecewise polytropic EOS Models employed in the present simulations. Model EOS name, $P_{\rm fid}$: the pressure at the fiducial density $\rho_{\rm fid} = 10^{14.7}\ \mathrm{g\,cm^{-3}}$, Γ_i (i = 1–3), and the maximum gravitational mass of spherical NSs for the given EOS. The first four EOSs are composed only of two pieces.

EOS	$\log_{10}P_{\rm fid}[\mathrm{dyne/cm^2}]$	Γ_1	Γ_2	Γ_3	$M_{\rm max}[M_\odot]$
15H	34.700	3.000	N/A	N/A	2.53
H	34.500	3.000	N/A	N/A	2.25
HB	34.400	3.000	N/A	N/A	2.12
B	34.300	3.000	N/A	N/A	2.00
H4	34.669	2.909	2.246	2.144	2.03
APR4	34.269	2.830	3.445	3.348	2.20

falls into the BH, forms a remnant disk, and becomes unbound from the system, i.e., ejecta. Evaluating the properties of the disk and the ejecta is essential for discussing resultant models of EM counterparts. Here we describe the method to evaluate these quantities. In the following, we will define the time of merger $t_{\rm merger}$ as the time when $0.01M_\odot$ of the NS matter falls into the apparent horizon.

At each time slice, we evaluate the remnant disk by the rest mass outside the apparent horizon, i.e., the remnant disk mass with the integral

$$M_{>\rm AH} \coloneqq \int_{r>r_{\rm AH}} \rho_* d^3x \tag{2}$$

where $r_{\rm AH} = r_{\rm AH}(\theta,\phi)$ denotes the coordinate radius of the apparent horizon and ρ_* is defined in Table I.

The unbound matter of the system, ejecta, is defined as the matter satisfying $-u_t > 1$, because in this paper we focus only on the dynamical ejecta, for which the thermal effect is minor. The mass of ejecta at each time slice is defined by the integral

$$M_{\rm eje} \coloneqq \int_{-u_t>1, r>r_{\rm AH}} \rho_* d^3x. \tag{3}$$

Assuming that the thermal energy of the ejecta is much smaller than the kinetic energy, the asymptotic kinetic energy of the ejecta, $T_{\rm eje}$, can be defined by

$$T_{\rm eje} \coloneqq \int_{-u_t>1, r>r_{\rm AH}} \rho_*(-u_t) d^3x. \tag{4}$$

Then the average velocity of the ejecta is estimated from the asymptotic kinetic energy $T_{\rm eje}$, and the ejecta mass $M_{\rm eje}$, as

$$v_{\rm eje} \coloneqq \sqrt{\frac{2T_{\rm eje}}{M_{\rm eje}}}. \tag{5}$$

Following the previous studies [32,33,38,45–47], we evaluate all these ejecta quantities at 10 ms after the onset of the merger.

2. Black hole parameters

During the inspiral or postmerger stage, the parameters of BHs are estimated from the quantities of the apparent horizons. If we assume that the spacetime near the apparent horizon is stationary, the equatorial circumferential radius $C_{\rm e}$ and the area of the apparent horizon $A_{\rm AH}$ can be approximated as [29]

$$C_{\rm e} = 4\pi M_{\rm BH}, \tag{6}$$

and

$$A_{\rm AH} = 8\pi M_{\rm BH}^2\left(1+\sqrt{1-\chi_{\rm BH}^2}\right). \tag{7}$$

Then BH mass $M_{\rm BH}$ and dimensionless spin parameter $\chi_{\rm BH}$ can be evaluated from Eqs. (6) and (7).

From the comparison of different estimations of the spin parameter, it has been found that the systematic error with this method to estimate the spin is much less than 0.01 [29,31,45]. Therefore, the spin parameter used in the paper for developing fitting formulas is accurate enough for our study.

3. Gravitational waves

To derive gravitational waveforms, we extract the Weyl scalar Ψ_4 at the coordinate radius of $D = 480M_\odot$ from the coordinate origin and extrapolate them to the null infinity with a method from the BH perturbation theory [76]. The gravitational waveforms $h_{\rm GW}$ are obtained from the time integration of the $l = |m| = 2$ spherical harmonics modes of Ψ_4. All the waveforms in this paper are shown for the observer along the z-axis. To reduce the nonphysical low-frequency components, we do not perform the time integration directly but adopt the method proposed by Reisswig and Pollney [77]. The retard time $t_{\rm ret}$ is approximately obtained by

$$t_{\rm ret} = t - D - 2m_0 \ln(D/m_0). \tag{8}$$

The GW spectrum is obtained as the sum of the Fourier components of the two polarizations of $l = |m| = 2$ modes:

$$\tilde{h}(f) = \sqrt{\frac{|\tilde{h}_+(f)|^2 + |\tilde{h}_\times(f)|^2}{2}}, \tag{9}$$

where

$$\tilde{h}_{+,\times}(f) = \int e^{2\pi i f t} h_{+,\times}(t) dt. \tag{10}$$

We use the normalized amplitude $f|\tilde{h}(f)|D/m_0$ as a function of a dimensionless frequency fm_0 to show the GW spectrum in the following plots.

D. Fitting formulas

Former studies give fitting formulas for $\hat{M}_{\rm rem}$ [38,47] and $\hat{M}_{\rm eje}$ [33,46]. In these fitting formulas, $\hat{M}_{\rm rem}$ and $\hat{M}_{\rm eje}$ are determined by the mass ratio Q, the dimensionless BH spin $\chi_{\rm BH}$, and the NS compactness $C_{\rm NS}$ except for the one derived in Ref. [33], which also depends on the value of $M_{\rm NS}/M_{\rm b}$. In Sec. III B we will demonstrate that this parametrization is sufficient for estimating $\hat{M}_{\rm rem}$ and $\hat{M}_{\rm eje}$.

(1) In Ref. [38], the fitting formula for the remnant mass (referred to as rem_2012) is determined as

$$\frac{M^{\rm rem}_{\rm fit,2012}}{M_{\rm b}} = \alpha(3Q)^{1/3}(1-2C_{\rm NS}) - \beta\frac{R_{\rm ISCO}}{R_{\rm NS}}, \tag{11}$$

$$= \alpha(3Q)^{1/3}(1-2C_{\rm NS}) - \beta r_{\rm ISCO}(\chi_{\rm BH})QC_{\rm NS}, \tag{12}$$

where α and β are determined by minimizing the χ-square (as defined in Eq. (23) below) of the fitting formula, $R_{\rm ISCO}$ is the radius of the innermost stable circular orbit (ISCO) of the remnant BH with $r_{\rm ISCO} = R_{\rm ISCO}/M_{\rm BH}$, and other quantities are defined in Table I. The ranges of the initial NS and BH parameters covered by the numerical simulations are $Q = 3$–7, $\chi_{\rm BH} = 0$–0.9, $C_{\rm NS} = 0.13$–0.18, and the best-fit model gives $\alpha \approx 0.288$ and $\beta \approx 0.148$. Here $R_{\rm ISCO}$ is given by

$$Z_1 = 1 + (1-\chi_{\rm BH})^{1/3} \times [(1+\chi_{\rm BH})^{1/3} + (1-\chi_{\rm BH})^{1/3}] \tag{13}$$

$$Z_2 = \sqrt{3\chi^2_{\rm BH} + Z_1^2} \tag{14}$$

$$\frac{R_{\rm ISCO}}{M_{\rm BH}} = 3 + Z_2 - {\rm sign}(\chi_{\rm BH})\sqrt{(3-Z_1)(3+Z_1+2Z_2)}, \tag{15}$$

as in Ref. [78].

(2) Reference [47] gives a modified fitting formula for the remnant mass (referred to as rem_2018)

$$\frac{M^{\rm rem}_{\rm fit,2018}}{M_{\rm b}} = \left[{\rm Max}\left(\alpha\frac{1-2C_{\rm NS}}{\eta^{1/3}} - \beta r_{\rm ISCO}\frac{C_{\rm NS}}{\eta} + \gamma, 0\right)\right]^{\delta}, \tag{16}$$

where η denotes the symmetric mass ratio $\eta = Q/(1+Q)^2$. The best fitting gives $\alpha = 0.406$, $\beta = 0.139$, $\gamma = 0.255$, $\delta = 1.761$ and the parameter space for the simulations was $Q = 1$–7, $\chi_{\rm BH} = -0.5$–0.9, $C_{\rm NS} = 0.13$–0.182 and $M_{\rm rem} \le 0.3M_{\rm b}$.

(3) Reference [33] gives the fitting formula for the ejecta mass (referred to as eje_2016) as

$$\frac{M^{\rm eje}_{\rm fit,2016}}{M_{\rm b}} = {\rm Max}\left[a_1 Q^{n_1}\frac{1-2C_{\rm NS}}{C_{\rm NS}} - a_2 Q^{n_2} r_{\rm ISCO}(\chi_{\rm eff}) + a_3\left(1-\frac{M_{\rm NS}}{M_{\rm b}}\right) + a_4, 0\right] \tag{17}$$

$$\chi_{\rm eff} = \chi_{\rm BH}\cos i_{\rm tilt} \tag{18}$$

In our simulations, the angle between the BH spin and the orbital angular momentum is $i_{\rm tilt} = 0$. The best-fit gives $a_1 = 4.464\times10^{-2}$, $a_2 = 2.269\times10^{-2}$, $a_3 = 2.431$, $a_4 = -0.4159$, $n_1 = 0.2497$, $n_2 = 1.352$, and the parameter space for simulations was $Q = 3$–7, $\chi_{\rm BH} = 0$–0.75, and $C_{\rm NS} = 0.138$–0.18 by fixing $M_{\rm NS} = 1.35M_\odot$ and changing EOS.

(4) Reference [46] gives a modified fitting formula for the ejecta mass (referred to as eje_2020)

$$\frac{M^{\rm eje}_{\rm fit,2020}}{M_{\rm b}} = a_1 Q^{n_1}\frac{1-2C_{\rm NS}}{C_{\rm NS}} - a_2 Q^{n_2} r_{\rm ISCO} + a_4. \tag{19}$$

The fitting results are $a_1 = 0.007116$, $a_2 = 0.001436$, $a_4 = -0.02762$, $n_1 = 0.8636$, $n_2 = 1.6840$, and the parameter space for simulations was the same as that of Ref. [33].

(5) Reference [33] also gives a fitting formula for the average ejecta velocity [cf., Eq. (5)] as a simple linear function of Q:

$$v^{\rm eje}_{\rm fit,2016} = (0.01533Q + 0.1907)c. \tag{20}$$

The definition of average ejecta velocity used to fit $v^{\rm eje}_{\rm fit,2016}$ is given by Eq. (B4) in Appendix B, which is not the same as $v_{\rm eje}$ given in Eq. (5).

E. Models

Table III lists BH-NS binary models and initial parameters used in our study. The models are labeled by EOS-$Q\chi_{\rm BH}M_{\rm NS}$, i.e., 15H-Q3a75M18 means the model with NS EOS "15H," mass ratio $Q = 3$, NS mass $M_{\rm NS} = 1.8M_\odot$, and dimensionless BH spin $\chi_{\rm BH} = 0.75$ aligned with the orbital angular momentum.

In Sec. III B, to verify our hypothesis that the normalized disk mass and ejecta mass only depend on $Q, \chi_{\rm BH}$, and $C_{\rm NS}$, we perform simulations by varying the NS mass with fixing these three parameters, and explore whether the differences of results among different models are within the range of numerical accuracy. To compare our results with previous ones, we choose three configurations of Q and $\chi_{\rm BH}$ as $(Q,\chi_{\rm BH}) = (3,0.5), (3,0.75)$ and (5,0.75). We study the models fixing the NS compactness with $C_{\rm NS} = 0.182$, but employing EOS models with two-pieces 15H, HB, and four-pieces EOS models H4 and APR4 [79–81] to vary the NS mass. Since the ejecta mass is small in the $C_{\rm NS} = 0.182$ cases, we also perform simulations with fixed compactness $C_{\rm NS} = 0.147$, with two-pieces EOS models 15H, H, B, and four-pieces EOS model APR4, for which we expect to get a larger disk and ejecta masses. In the following, we will refer to the models with fixed compactness $C_{\rm NS} = 0.147$ and $C_{\rm NS} = 0.182$ as C147 and C182, respectively.

We note that the purpose of studying the models with four-pieces EOS is to test whether the simplified two-pieces EOSs can be used to accurately describe the NS tidal disruption in BH-NS mergers and to test how the difference in the detailed internal structure of the NS can change

TABLE III. Parameters of initial data and grid structure for all the models studied in this paper. The model name contains the EOS employed, the mass ratio (Q), and the dimensionless spin of the black hole $\chi_{\rm BH}$. $M_{\rm NS}$, $M^{\rm b}_{\rm NS}$, $R_{\rm NS}$, $C_{\rm NS}$, and $M_{\rm BH,0}$ are the initial NS mass, NS restmass, NS radius, NS compactness, and BH mass, respectively. $m_0\Omega_0$ is the dimensionless initial orbital angular velocity of the system. L is the box size of the simulation, Δx is the grid spacing at the finest level, and $R_{\rm diam}/\Delta x$ is the grid number within the semimajor diameter of the NS. N denotes the grid resolution of the simulation. The table contains three parts. The first part shows the parameters for the fixed value of the NS mass as $M_{\rm NS} = 1.8M_\odot$, the second and third parts show the parameters for the fixed values of $C_{\rm NS} = 0.182$ and 0.147, respectively. Δx and $R_{\rm diam}/\Delta x$ are calculated with the grid resolution of $N = 82$.

Model	EOS	$M_{\rm NS}[M_\odot]$	$M^{\rm b}_{\rm NS}[M_\odot]$	$R_{\rm NS}$[km]	$C_{\rm NS}$	Q	$M_{\rm BH,0}[M_\odot]$	$\chi_{\rm BH}$	$m_0\Omega_0$	Δx[m]	$R_{\rm diam}/\Delta x$	L[km]	N
15H-Q3a5M18	15H	1.800	2.022	13.70	0.194	3.0	5.400	0.50	0.0377	204	134	8553	62, 82
H-Q3a5M18	H	1.800	2.056	12.14	0.219	3.0	5.400	0.50	0.0377	180	135	7565	62, 82
15H-Q3a75M18	15H	1.800	2.022	13.70	0.194	3.0	5.400	0.75	0.0375	204	134	8553	62, 82, 102
H-Q3a75M18	H	1.800	2.056	12.14	0.219	3.0	5.400	0.75	0.0375	180	135	7565	62, 82
B-Q3a75M18	B	1.800	2.103	10.55	0.252	3.0	5.400	0.75	0.0375	163	129	6842	62, 82
15H-Q5a75M18	15H	1.800	2.022	13.70	0.194	5.0	9.000	0.75	0.0445	203	134	8523	62, 82
H-Q5a75M18	H	1.800	2.056	12.14	0.219	5.0	9.000	0.75	0.0445	180	135	7565	62, 82
15H-Q3a5M1691	15H	1.691	1.884	13.72	0.182	3.0	5.073	0.50	0.0369	204	135	8553	62, 82
HB-Q3a5M1428	HB	1.428	1.590	11.59	0.182	3.0	4.284	0.50	0.0353	171	136	7182	62, 82
15H-Q3a75M1691	15H	1.691	1.884	13.72	0.182	3.0	5.073	0.75	0.0367	204	135	8553	62, 82
HB-Q3a75M1428	HB	1.428	1.590	11.59	0.182	3.0	4.284	0.75	0.0351	171	136	7182	62, 82, 102
APR4-Q3a75M1366	APR4	1.366	1.522	11.08	0.182	3.0	4.098	0.75	0.0358	164	135	6901	62, 82
H4-Q3a75M1651	H4	1.651	1.836	13.40	0.182	3.0	4.950	0.75	0.0356	199	135	8347	62, 82
15H-Q5a75M1691	15H	1.691	1.884	13.72	0.182	5.0	8.455	0.75	0.0411	204	135	8553	62, 82, 102
HB-Q5a75M1428	HB	1.428	1.590	11.59	0.182	5.0	7.140	0.75	0.0404	171	136	7182	62, 82, 102
H-Q3a5M1220	H	1.220	1.327	12.26	0.147	3.0	3.660	0.50	0.0351	182	135	7639	62, 82
B-Q3a5M1092	B	1.092	1.187	10.97	0.147	3.0	3.276	0.50	0.0357	163	135	6842	62, 82
15H-Q3a75M1363	15H	1.363	1.484	13.69	0.147	3.0	4.089	0.75	0.0349	203	135	8523	62, 82
H-Q3a75M1220	H	1.220	1.327	12.26	0.147	3.0	3.660	0.75	0.0349	182	135	7639	62, 82, 102
B-Q3a75M1092	B	1.092	1.187	10.97	0.147	3.0	3.276	0.75	0.0356	163	135	6842	62, 82
APR4-Q3a75M1094	APR4	1.094	1.190	10.99	0.147	3.0	3.282	0.75	0.0356	163	135	6842	62, 82
H-Q5a75M1220	H	1.220	1.327	12.26	0.147	5.0	6.100	0.75	0.0449	182	135	7639	62, 82
B-Q5a75M1092	B	1.092	1.187	10.97	0.147	5.0	5.460	0.75	0.0451	163	135	6842	62, 82

the results of the simulations. Two-pieces polytropes are simplified EOSs, which are typically employed in addressing less massive NSs. It can be proved that for an NS with mass less than $1.4M_\odot$, its central density is relatively low, which means the EOS at higher density plays a minor role. Hence, two-pieces and four-pieces EOS should provide approximately the same results for the C147 models. On the other hand, for the C182 models, the NS structure in high-density regions can be sensitive to the values of Γ_2 and Γ_3. Therefore, it is necessary to perform simulations with both two-pieces and four-pieces EOS models to test whether our conclusions can be applied despite the detailed structure of the NS.

In Sec. III C, we further perform simulations with a high value of $M_{\rm NS} = 1.8M_\odot$ while fixing Q and $\chi_{\rm BH}$ to check the validity of the fitting formulas with large values of NS compactness. As we demonstrate in Sec. III B that merger dynamics depends on $M_{\rm NS}$ and $R_{\rm NS}$ approximately only through the NS compactness ($C_{\rm NS} = M_{\rm NS}/R_{\rm NS}$), it is an interesting exploration to see the dependence of the merger dynamics by varying the compactness of NSs while fixing $M_{\rm NS}$, i.e., by changing the EOS of NSs. We choose EOSs, 15H, H, and B, with the compactness varying from 0.194 to 0.252.

To evaluate the validity of fitting formulas, we calculate the χ-square of their fittings, with the estimation of numerical error from both Refs. [33,38] and our study. Numerical simulations are performed with grid resolutions $N = 62$, 82 for all the models, and $N = 102$ for some of them (see Appendix A) to estimate the numerical errors due to the finite grid resolution. We take $N = 82$ as the fiducial resolution of our simulations and other results are summarized in the Appendix A.

III. RESULTS

We present our numerical results in this section, focusing primarily on their dependence on the NS compactness, the mass ratio, and the dimensionless BH spin. After we describe an overview of the BH-NS merger process in Sec. III A, we summarize the result for the case of a fixed NS compactness in Sec. III B, and then, for the case of massive and compact NSs in Sec. III C. The numerical results are shown in Tables IV–VI, respectively.

TABLE IV. Characteristic physical quantities for the model with $C_{\rm NS} = 0.182$. $\hat{M}_{\rm rem}$ is the normalized remnant mass for the matter located outside the apparent horizon, $\hat{M}_{\rm eje}$ is the ejecta mass during the merger, normalized by the baryon mass of the NS. $f_{\rm cut}m_0$ is the normalized cutoff frequency. $T_{\rm eje}$ and $v_{\rm eje}$ are the asymptotic kinetic energy and velocity of the ejecta. $\chi^f_{\rm BH}$ and $M^f_{\rm BH}$ are the dimensionless spin and mass of BHs after the merger. Models with EOS "B" are taken from Ref. [45], with $C_{\rm NS} = 0.1819$, $M_{\rm NS} = 1.35M_\odot$, and $N = 50$. Some values are N/A since Ref. [45] does not provide them. All physical quantities are evaluated at 10 ms after the onset of merger. The grid resolution is $N = 82$.

Model ID		EOS	$\hat{M}_{\rm rem}$	$\hat{M}_{\rm eje}$	$f_{\rm cut}m_0$	$T_{\rm eje}$ [erg]	$v_{\rm eje}[c]$	$\chi^f_{\rm BH}$	$M^f_{\rm BH}[M_\odot]$
1	Q3a5	15H	0.052	0.0015	0.079	5.8×10^{49}	0.15	0.77	6.48
2		HB	0.047	0.0015	0.079	5.3×10^{49}	0.16	0.77	5.48
	Ref. [45]	B	0.033	N/A	N/A	N/A	N/A	0.77	N/A
3	Q3a75	15H	0.12	0.0046	0.071	2.3×10^{50}	0.18	0.87	6.37
4		HB	0.12	0.0059	0.069	2.8×10^{50}	0.18	0.87	5.38
5		APR4	0.12	0.0065	0.070	3.1×10^{50}	0.19	0.87	5.15
6		H4	0.13	0.0042	0.069	2.3×10^{50}	0.18	0.87	6.22
	Ref. [45]	B	0.10	N/A	N/A	N/A	N/A	0.86	N/A
7	Q5a75	15H	0.037	0.0047	0.101	2.8×10^{50}	0.19	0.85	9.81
8		HB	0.036	0.0054	0.101	2.8×10^{50}	0.19	0.85	8.29
	Ref. [45]	B	0.021	N/A	N/A	N/A	N/A	0.85	N/A

TABLE V. Characteristic physical quantities for the models with $C_{\rm NS} = 0.147$. Models with EOS "H4" are taken from Ref. [32], with $C_{\rm NS} = 0.147$, $M_{\rm NS} = 1.35M_\odot$, and $N = 60$. $T_{\rm eje}$ and $v_{\rm eje}$ from Ref. [32] are not listed in the table since we use different definitions, which will be discussed in Appendix. B. $f_{\rm cut}m_0$ is also not listed since Ref. [32] does not provide it. Other quantities have the same definitions as in Table IV.

Model ID		EOS	$\hat{M}_{\rm rem}$	$\hat{M}_{\rm eje}$	$f_{\rm cut}m_0$	$T_{\rm eje}$ [erg]	$v_{\rm eje}[c]$	$\chi^f_{\rm BH}$	$M^f_{\rm BH}[M_\odot]$
9	Q3a5	H	0.16	0.024	0.040	9.4×10^{50}	0.18	0.76	4.59
10		B	0.16	0.022	0.041	8.4×10^{50}	0.19	0.76	4.11
	Ref. [32]	H4	0.16	0.02	N/A	N/A	N/A	0.76	5.07
11	Q3a75	15H	0.22	0.030	0.038	1.3×10^{51}	0.18	0.87	5.07
12		H	0.21	0.030	0.039	1.2×10^{51}	0.19	0.87	4.54
13		B	0.21	0.031	0.039	1.2×10^{51}	0.19	0.87	4.07
14		APR4	0.21	0.031	0.039	1.2×10^{51}	0.19	0.87	4.07
	Ref. [32]	H4	0.22	0.03	N/A	N/A	N/A	0.88	4.99
15	Q5a75	H	0.21	0.040	0.059	2.2×10^{51}	0.21	0.83	6.93
16		B	0.21	0.039	0.061	2.0×10^{51}	0.22	0.83	6.21
	Ref. [32]	H4	0.22	0.03	N/A	N/A	N/A	0.83	7.65

TABLE VI. Characteristic physical quantities for the model with $M_{\rm NS} = 1.8M_\odot$. Other quantities have the same definitions as in Table IV.

	EOS	$\hat{M}_{\rm rem}$	$\hat{M}^{2012}_{\rm fit}$	$\hat{M}^{2018}_{\rm fit}$	$\hat{M}_{\rm eje}$	$\hat{M}^{2016}_{\rm fit}$	$\hat{M}^{2020}_{\rm fit}$	$T_{\rm eje}[{\rm erg}]$	$v_{\rm eje}[c]$	$\chi^f_{\rm BH}$	$M^f_{\rm BH}[M_\odot]$
Q3a0.5	15H	0.014	1.88×10^{-3}	0.0117	3.3×10^{-4}	0	0	1.0×10^{49}	0.13	0.770	6.95
	H	5.8×10^{-5}	0	0	1.1×10^{-6}	0	0	3.8×10^{46}	0.13	0.761	6.93
Q3a0.75	15H	0.081	0.0945	0.0779	1.5×10^{-3}	4.56×10^{-3}	1.49×10^{-3}	6.9×10^{49}	0.16	0.870	6.83
	H	8.9×10^{-3}	0.0283	0.0310	1.1×10^{-4}	5.48×10^{-3}	0	3.7×10^{48}	0.14	0.866	6.90
	B	1.1×10^{-5}	0	7.73-04	5.3×10^{-7}	0.0187	0	2.3×10^{46}	0.15	0.858	6.87
Q5a0.75	15H	6.3×10^{-3}	0	0.0244	9.2×10^{-4}	0	0	5.6×10^{49}	0.18	0.846	10.48
	H	9.5×10^{-6}	0	6.58×10^{-6}	2.6×10^{-6}	0	0	1.4×10^{47}	0.17	0.844	10.47

A. Overview of the merger

First we briefly describe an overview of the BH-NS merger process in our numerical simulations. Broadly speaking, we find the same features as for $M_{\rm NS} \approx 1.4 M_\odot$ studied in the previous works [22–26,28–33,35–42,45,82–92]: The BH-NS mergers can have two types of fate. One is that the NS is tidally disrupted by the BH, and subsequently, an accretion disk is formed around the remnant BH and a part of the NS matter is ejected as the dynamical ejecta; the other is that the NS simply plunges into the BH with no tidal disruption and no mass ejection. In the following, we pay attention only to the former case because it can provide a lot of information about the BH-NS systems through the cutoff frequency and EM counterparts powered by the ejecta.

The condition of tidal disruption can be obtained by comparing the ISCO radius $R_{\rm ISCO}$ and the mass-shedding radius $R_{\rm dis}$. If $R_{\rm ISCO} \le R_{\rm dis}$, the NS can be tidally disrupted before it is swallowed into the BH. Assuming Newton's gravity for simplicity, we have [21]

$$\frac{R_{\rm dis}}{R_{\rm ISCO}} \propto \frac{1}{C_{\rm NS} Q^{2/3} r_{\rm ISCO}(\chi_{\rm BH})}. \tag{21}$$

This ratio approximately separates the two types of final fates mentioned above. If the ratio is larger than unity, the NS is expected to be tidally disrupted by the BH. Otherwise, the BH-NS binaries encounter an ISCO before reaching mass shedding limit, NS will simply plunge into the BH with no tidal disruption. Thus, the significance of the tidal disruption appears to depend on Q, $\chi_{\rm BH}$, and $C_{\rm NS}$, and the tidal disruption is less relevant for larger values of Q and $C_{\rm NS}$ and smaller value of $\chi_{\rm BH}$ since $R_{\rm ISCO}$ decreases as $\chi_{\rm BH}$ increases. However, the relation of this ratio may be modified in general relativity, in particular for high-mass NSs for which the general relativistic effect is enhanced. The dependence of ejecta mass and the remnant mass on these three parameters as well as on the NS mass are discussed in detail in Secs. III B and III C.

Figure 1 shows the snapshot of the rest-mass density profile, unbound matter, and the apparent horizon at selected time slices for model HB-Q5a75M1428. The separation between the NS and BH decreases due to GW emission, and after it reaches the tidal disruption radius, the NS is tidally disrupted (see the top panels in Fig. 1). While most of the disrupted NS matter is swallowed by the BH, a fraction of the matter will gain angular momentum by gravitational torque to form the tidal tail which remains outside the BH. The gravitationally-bounded matter in the tidal tail gradually falls back and forms a remnant disk around the remnant BH (see the bottom panels in Fig. 1), while the matter in the outer part of the tidal tail becomes dynamical ejecta.

Figure 2 shows the time evolution for the rest mass of the matter located outside the BH for three models, H-Q3a75M1220, 15H-Q3a5M18, and H-Q5a75M18 models, which represent the cases with significant tidal disruption, the intermediate case, and no tidal disruption, respectively. It shows that in tidal disruptions, indeed most of the NS matter is swallowed by the BH soon after the onset of the merger, i.e., within ∼1 ms, and the rest mass of the matter remaining outside the BH depends strongly on the binary parameter. For the case with significant tidal disruption (H-Q3a75M1220), 1%–20% of the mass surrounds the BH to form a remnant disk, but only less than 0.01% of matter remains outside the BH after the merger for the no tidal disruption case (H-Q5a75M18).

At the time of the merger, a fraction of the matter outside the BH becomes gravitationally unbound, i.e., the dynamical ejecta. The region in Fig. 1 surrounded by the dashed curves denotes the matter with gravitationally unbound orbits. Figure 1 shows that the ejecta is formed around the outer edge of the tidal tail. The time evolution of the ejecta mass is shown in Fig. 3. The ejecta are formed within the dynamical timescale (∼1 ms) after the onset of the merger, and, as is the case for the remnant matter located outside the BH, the amount of the ejecta depends strongly on the binary parameters.

B. Fixed compactness case

1. Properties of remnant disks and ejecta

We list the key results of the simulations for C182 and C147 models in Tables IV and V, respectively. We also include the results for $\hat{M}_{\rm rem}$ and $\hat{M}_{\rm eje}$ with the same compactness from Refs. [32,45]. Tables IV and V show that $\hat{M}_{\rm rem}$ increases as $\chi_{\rm BH}$ increases, and as the compactness $C_{\rm NS}$ and the mass ratio Q decreases. This is consistent with the predictions given in Sec. III A. However, we note that the dependence of $\hat{M}_{\rm rem}$ on Q is rather weak in the case of the lower compactness $C_{\rm NS} \approx 0.147$, which deviates from the naive prediction of Newton approximation shown in Eq. (21). This weaker dependence is also found and an interpretation for this is described in Ref. [34].

From Table V and IV, it is found that $\hat{M}_{\rm eje}$ increases as $\chi_{\rm BH}$ increases and as $C_{\rm NS}$ decreases. This is the same dependence as $\hat{M}_{\rm rem}$. However, being different from $\hat{M}_{\rm rem}$, $\hat{M}_{\rm eje}$ increases as Q increases for the lower compactness $C_{\rm NS} \approx 0.147$. This has also been found in the previous works [29,32,33,35,38,41,42]. This implies that the ejecta mass depends more strongly on the dynamical process of the tidal disruption than the remnant mass, and indicates that the dynamics of the tidally disrupted matter in the vicinity of the BH plays a key role in determining the ejecta mass.

Figure 4 compares the values of $\hat{M}_{\rm rem}$ among the models with the same values of Q, $\chi_{\rm BH}$, and $C_{\rm NS}$ but with different NS mass $M_{\rm NS}$, i.e., with different NS EOSs. The error bars are taken to be the discrepancy of the results between $N = 62$ and $N = 82$ runs of the same model. Hydrodynamic quantities do not always show monotonic dependency on

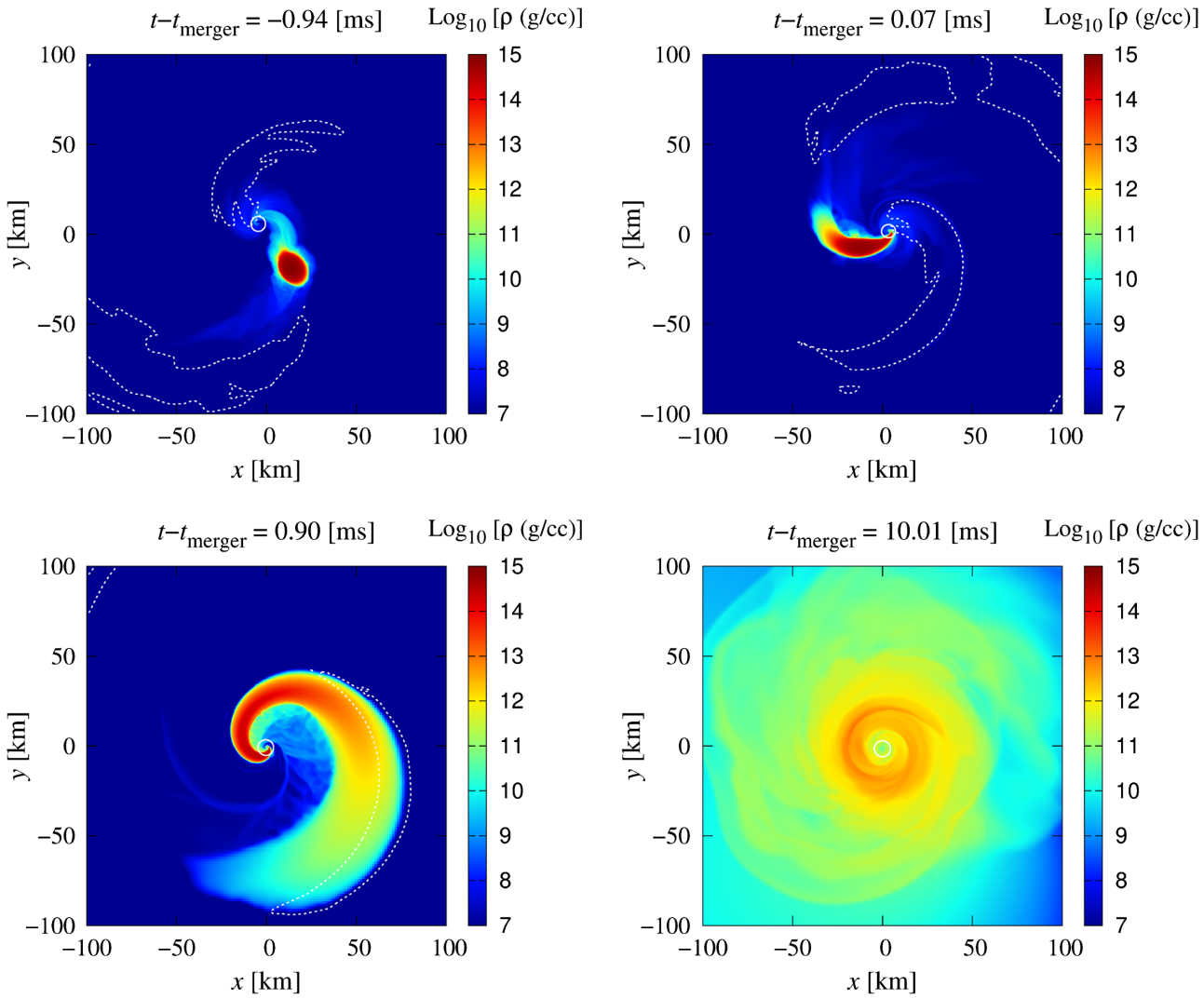

FIG. 1. Time evolution of the rest-mass density profile for model HB-Q3a75M1428 with $N = 82$ run at $t - t_{\rm merger} \approx -0.94$ ms (top left), 0.07 ms (top right), 0.90 ms (bottom left), and 10.01 ms (bottom right). The white circle indicates the apparent horizon. The white dashed lines show the region of unbound components in which the relation $-u_t \geq 1$ is satisfied.

the grid resolution and it is difficult to evaluate the error by checking the convergence. Therefore we take the error estimation method shown above. We note that the discrepancies between $N = 82$ and $N = 102$ results are mostly smaller than those between $N = 62$ and $N = 82$ results (see Appendix. A). If the range of error bars for different models with the same values of $\chi_{\rm BH}, Q$, and $C_{\rm NS}$ overlaps, we consider that the results are in agreement within the range of the accuracy.

It is shown that, within the numerical accuracy, $\hat{M}_{\rm rem}$ with the same values of $Q, \chi_{\rm BH}$, and $C_{\rm NS}$ agrees with each other regardless of their different NS masses. We also find from Tables IV and V that the dimensionless spin of the remnant BH, $\chi^f_{\rm BH}$, is approximately the same among the models with the same initial values of $Q, \chi_{\rm BH}$, and $C_{\rm NS}$. This indicates that the BH swallows approximately the same amount of the mass and angular momentum normalized by $M_{\rm NS}$. These results show that $\hat{M}_{\rm rem}$ and the radius at which the NS tidal disruption occurs depends sensitively on $Q, \chi_{\rm BH}$, and $C_{\rm NS}$ while $M_{\rm NS}$ plays a role only in scaling the system.

Figure 5 shows the results for the ejecta mass, with its error bar defined in the same way as Fig. 4. $\hat{M}_{\rm eje}$ with the same values of $Q, \chi_{\rm BH}$, and $C_{\rm NS}$ also agrees with each other. The results show that $\hat{M}_{\rm eje}$ also depends sensitively on Q, $\chi_{\rm BH}$, and $C_{\rm NS}$ but only minorly on $M_{\rm NS}$.

It is worth noting that the values of $\hat{M}_{\rm rem}$ and $\hat{M}_{\rm eje}$ for the models which employ the four-pieces EOSs (model ID = 5, 6, and 14) are also approximately in agreement with the results for the models which employ the two-pieces EOSs with the same values of $Q, \chi_{\rm BH}$, and $C_{\rm NS}$. This implies that the detailed structure, i.e., the value of Γ_2 in Table II, has only a minor effect on the results of $\hat{M}_{\rm rem}$ and $\hat{M}_{\rm eje}$. This conclusion also justifies us to study NSs with $M_{\rm NS} = 1.8 M_\odot$ using two-pieces polytropes in Sec. III C.

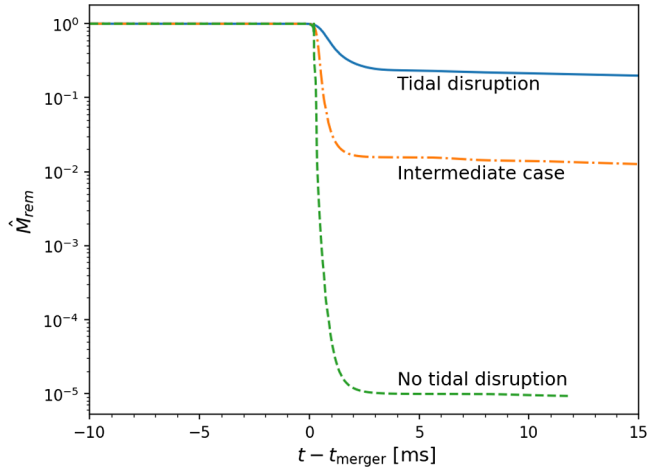

FIG. 2. Time evolution of $\hat{M}_{\rm rem}$ for representative models, H-Q3a75M1220, 15H-Q3a5M18, and H-Q5a75M18 (solid, dot-dashed, and dashed lines, respectively). Each model represents the cases with significant tidal disruption, the intermediate situation, and no tidal disruption, respectively.

The fitting formula for the ejecta mass, Eq. (17), given in Ref. [33] includes not only $C_{\rm NS}$, Q, and $\chi_{\rm BH}$, but also the specific binding energy. Though the binding energy may physically have influence on the result, it is still consistent with our results. Since the specific binding energy can be well approximated as a function of the NS compactness $C_{\rm NS}$ (e.g., Ref. [93]), Eq. (17) can be effectively approximated as a function of only $C_{\rm NS}$, Q, and $\chi_{\rm BH}$. Also, we find that the variation of the specific binding energy term in our parameter space is nevertheless less than the estimated errors in our simulations (around 10%).

Figure 6 shows the average ejecta velocity $v_{\rm eje}$ and their error bars. Broadly speaking, $v_{\rm eje}$ increases with Q and

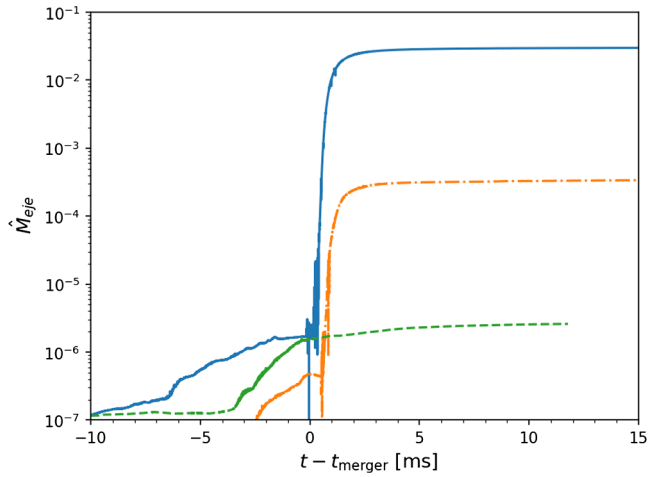

FIG. 3. Time evolution of $\hat{M}_{\rm eje}$ for the same models as in Fig. 2. The y-axis shows the normalized ejecta mass. The tiny amount of ejecta before and right after the merger is due to the mass conservation error around the NS atmosphere.

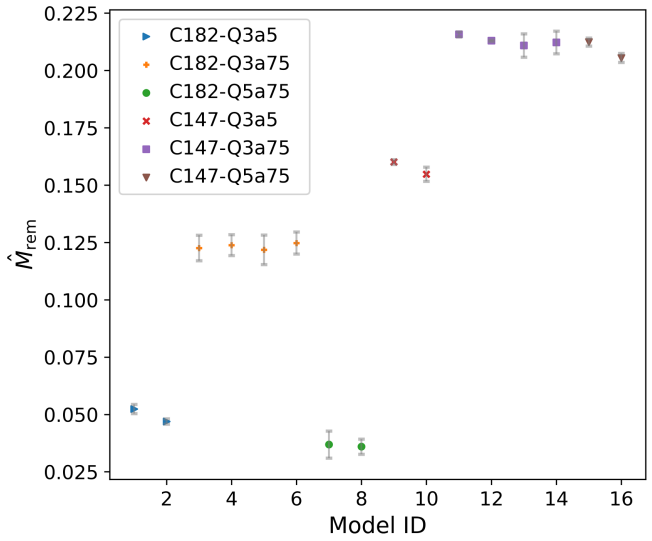

FIG. 4. The values of $\hat{M}_{\rm rem}$ for the models with $C_{\rm NS} = 0.182$ and 0.147. The models with the same values of $\chi_{\rm BH}$, Q, and $C_{\rm NS}$ but with different NS mass $M_{\rm NS}$ are grouped with the same colors. The error bar of each model is determined by the difference between $N = 62$ and $N = 82$ results. Model ID corresponds to the column model ID in Tables IV and V.

depends weakly on other parameters. This is consistent with the results of the previous studies for $M_{\rm NS} \approx 1.4 M_\odot$ [32,33,35,89], which is also described in fitting formula of Eq. (20). As is the case for $\hat{M}_{\rm rem}$ and $\hat{M}_{\rm eje}$, given the same values of Q, $\chi_{\rm BH}$, and $C_{\rm NS}$, the values of $v_{\rm eje}$ for different models approximately agree with each other within the numerical accuracy.

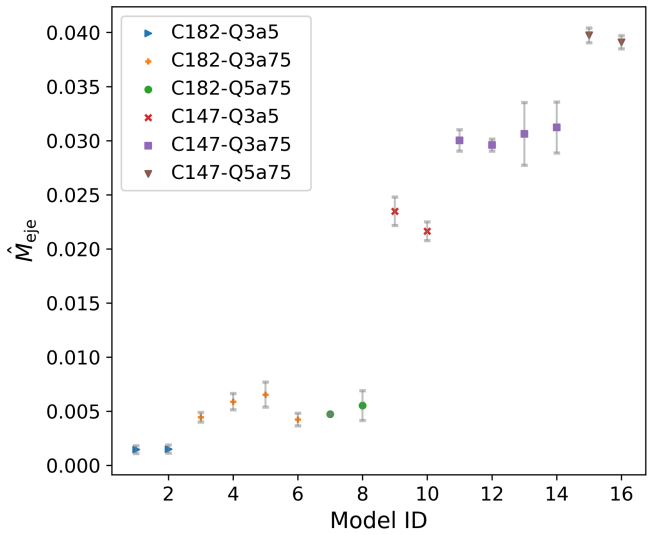

FIG. 5. The values of $\hat{M}_{\rm eje}$ for models with $C_{\rm NS} = 0.182$ and 0.147. The models with the same values of $\chi_{\rm BH}$, Q, and $C_{\rm NS}$ but with different NS mass $M_{\rm NS}$ are grouped with the same colors. The error bar of each model is determined by the difference between $N = 62$ and $N = 82$ results. Model ID corresponds to the column model ID in Tables IV and V.

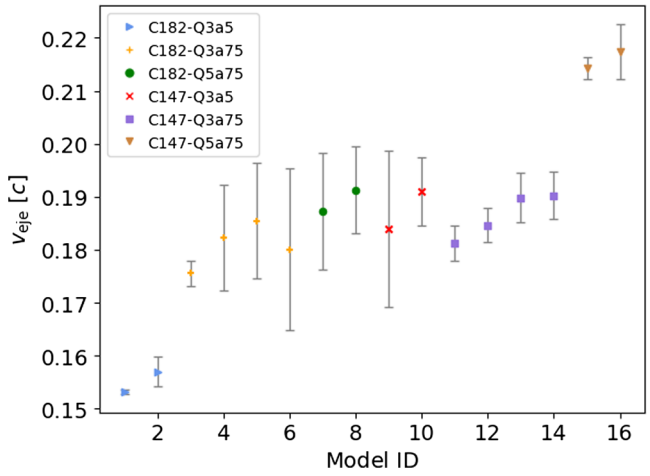

FIG. 6. The value of v_{eje} at 10 ms after the merger for models with $C_{NS} = 0.182$ and 0.147. The models with the same values of χ_{BH}, Q, and C_{NS} but with different NS mass M_{NS} are grouped with the same colors. The error bar of each model is determined by the difference between $N = 62$ and $N = 82$ results. Model ID corresponds to the column model ID in Tables IV and V.

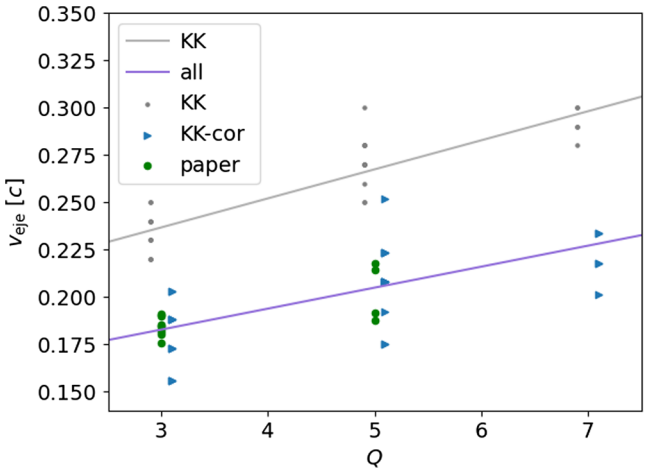

FIG. 7. Original average ejecta velocity in Ref. [33], corrected velocity $v_{eje,cor}$, and v_{eje} obtained in this paper as functions of mass ratio Q. "KK" denotes the data obtained from Ref. [33], "KK-cor" denotes the same data as "KK" but with the gravitational potential energy correction, $v_{eje,cor}$, "paper" denotes the data newly obtained in this paper. The line with a label "KK" denotes the fitting formula obtained in the previous study [33] [Eq. (20)]. The line with the label "all" denotes the fitting formula obtained by employing both data of "KK-cor" and "paper" [Eq. (22)]. The data points are slightly shifted in x-direction to make different sets of points separated.

The coefficients of the fitting formula of Eq. (20) given in Ref. [33] were obtained by fitting the average ejecta velocity $v_{eje,old}$ obtained by various configurations of BH-NS binaries. They assumed a linear relation between $v_{eje,old}$ and Q: $v_{eje,old} = (a_1 Q + a_2)c$, and used the least squares fitting to derive the coefficients a_1 and a_2. However, the definition of $v_{eje,old}$ in Ref. [33], which is different from the present definition in Eq. (5), did not take into account the gravitational potential. Thus, the value of $v_{eje,old}$ can be overestimated.

Here, we correct the effect of the gravitational potential energy in the data summarized in Ref. [33] by employing the method introduced in Ref. [34], and recalibrate the ejecta-velocity fitting formula employing those corrected data as well as the results obtained in this paper. Our method to correct the ejecta velocity $v_{eje,cor}$ is described in Appendix B. We note that, since the estimated value of the ejecta velocity for the models with small ejecta mass is not reliable, they employed only the models with $\hat{M}_{eje} > 0.003$. In this paper, we restrict the models in the same manner.

By employing all the data, including $v_{eje,cor}$ in Ref. [33] and v_{eje} in this paper, we obtain the fitting formula as

$$v_{eje,fit} = (0.01108Q + 0.1495)c. \tag{22}$$

Figure 7 shows that the average ejecta velocity in Ref. [33] is generally larger than v_{eje} obtained in this paper, while after correction, $v_{eje,cor}$ is generally closer to v_{eje}. This indeed shows that the values of $v_{eje,old}$ in Ref. [33] are overestimated by neglecting the effect of the gravitational potential energy. The largest relative fitting error of the fitting formula is around 10% for Eq. (20) and is around 18% for Eq. (22). On the other hand, the relative numerical error of v_{eje} in this paper estimated from the different resolution runs is around 10%. This implies that there is a approximate linear relation between v_{eje} and Q. It may indicate that the ejecta velocity is not only determined by the mass ratio Q, but also influenced by other parameters, such as the BH spin, NS compactness, and initial spin misalignment angle.

Figure 8 shows the velocity distributions of the ejecta normalized by its mass for selected models. The distributions are evaluated at 10 ms after the onset of the merger. The models shown in the figure are 15H-Q3a75M1691 and HB-Q3a75M1428 which have $(Q, \chi_{BH}, C_{NS}) = (3, 0.75, 0.182)$ in common, and H-Q5a75M1220 and B-Q5a75M1092 which have $(Q, \chi_{BH}, C_{NS}) = (5, 0.75, 0.147)$ in common. The distributions we obtained from our simulations show similar features to those obtained by Refs. [32,36,89]; they peak at $v_{eje} \approx 0.1c$–$0.3c$ and have a steep cutoff for both the lower and higher velocity sides. The models with the same values of (Q, χ_{BH}, C_{NS}) essentially show the same distributions having a peak at $v_{eje} \approx 0.15c$ and $0.2c$ for the models with $(Q, \chi_{BH}, C_{NS}) = (3, 0.75, 0.182)$ and (5,0.75,0.147), respectively. The NS mass M_{NS} does not play a role in changing the result significantly.

We also perform a careful resolution study in this paper for the ejecta velocity distribution and find a result worthy of remark. Figure 9 shows the ejecta velocity distribution for model H-Q3a75M1220 with resolutions N62, N82, and N102. It shows that for relatively low values of the ejecta

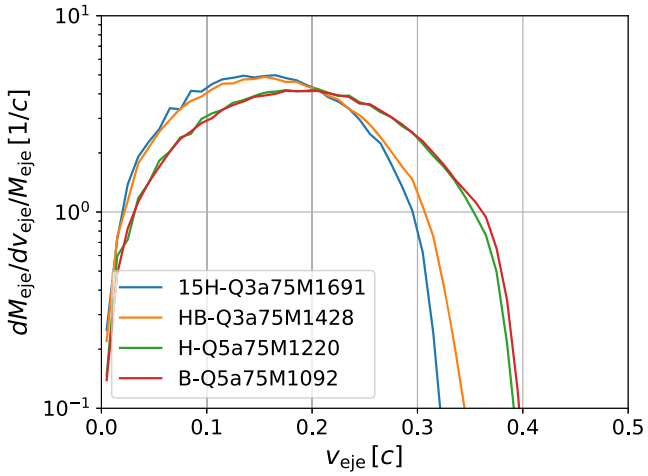

FIG. 8. Ejecta velocity distributions normalized by the ejecta mass for selected models. The models 15H-Q3a75M1691 and HB-Q3a75M1428 have $(Q, \chi_{\rm BH}, C_{\rm NS}) = (3, 0.75, 0.182)$ in common, and the models H-Q5a75M1220 and B-Q5a75M1092 have $(Q, \chi_{\rm BH}, C_{\rm NS}) = (5, 0.75, 0.147)$ in common. The models with the same values of $(Q, \chi_{\rm BH}, C_{\rm NS})$ approximately show the same distributions.

velocity convergence is achieved. However, for the high-velocity side with $\gtrsim 0.3c$ the convergence is not fully achieved. Specifically, for higher grid resolutions, more matter is present for the higher velocity side. Our interpretation for this is that with the higher grid resolution, the surface of the one-armed spiral, where the high-velocity ejecta exists, is better resolved and the pressure gradient plays a role in additionally accelerating the matter there.

2. *Properties of gravitational waves*

The location of the cutoff frequency in the amplitude of the GW spectrum at $f \gtrsim 1$ kHz contains rich information on the last stage of the inspiral phase and mainly depends on the orbital frequency of the tidal disruption [21,94,95]. If the NS is not tidally disrupted, the GW spectrum is characterized by the inspiral, merger, and ringdown waveforms, in which case the gravitational waveforms are nearly identical to those for binary BH mergers [96]. When tidal disruption happens, the wave amplitude quickly decreases before the ringdown phase, and the wave amplitude by the inspiral motion shuts down. This is because in the tidal disruptions, the NS matter becomes less dense and diffused, and the excitation of the quasinormal modes is suppressed by the phase cancellation [29,97–99]. The GW spectra in tidal disruptions are characterized by their damping above the cutoff frequency, $f_{\rm cut}$. To quantify $f_{\rm cut}$, previous studies fit the GW spectra by a function with seven parameters and define $f_{\rm cut}$ as one of the parameters [29,31,45]. However, these two definitions are not robust because the fitting formula is not flexible enough.

For $f \to 0$, $f|h(f)|$ is proportional to $f^{-1/6}$ and can be approximated by the quadrupole formula $fh_{\rm quad}(f)$ with the point-particle approximation and the binary motion is determined by Newtonian gravity (e.g., Ref. [100]). Therefore, we determine the value of $f_{\rm cut}$ to be the value of the intersection of the half of the GW spectrum obtained by the quadrupole formula and the one obtained from simulations; see Fig. 10 as an example.

Figure 11 shows the normalized cutoff frequency $f_{\rm cut}m_0$ and its error bars for models with the same values of Q, $\chi_{\rm BH}$, and $C_{\rm NS}$, and different EOSs. As in the cases of $M_{\rm rem}$ and $M_{\rm eje}$ (see Sec. III B 1), the error bars of $f_{\rm cut}m_0$ are also taken to be the discrepancies of the results between $N = 62$ and $N = 82$ runs. By comparing the models with different values of Q or $\chi_{\rm BH}$ or $C_{\rm NS}$, the figure shows that larger compactness $C_{\rm NS}$ and higher mass ratio Q induce higher

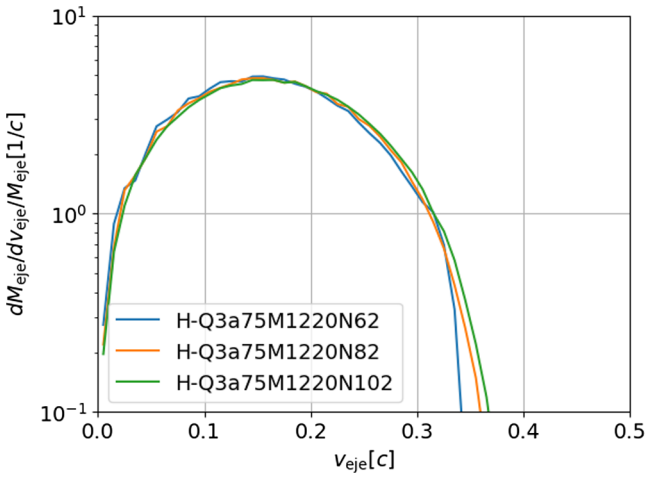

FIG. 9. Ejecta velocity distributions normalized by the ejecta mass for model 15H-Q3a75M18 with resolutions N62, N82, and N102. For the higher resolutions, the distribution is extended to the higher velocity side.

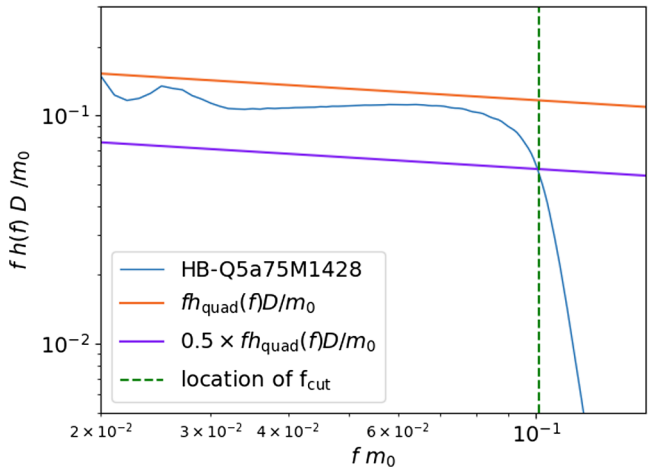

FIG. 10. The example that shows how we determine the value of $f_{\rm cut}m_0$. The blue curve is the GW spectrum obtained from model HB-Q5a75M1428, and the purple line is half of the GW spectrum obtained from the quadrupole formula. We identify the intersection frequency as the value of the cutoff frequency $f_{\rm cut}m_0$.

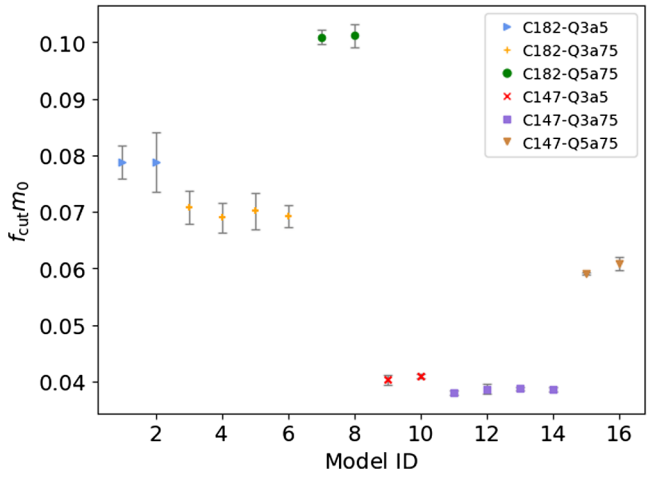

FIG. 11. The normalized cutoff frequency $f_{\rm cut}m_0$ for models with the same values of Q, $\chi_{\rm BH}$, $C_{\rm NS}$, and different EOSs. The error bar of each model is taken to be the discrepancy of the results between $N = 62$ and $N = 82$ runs. Model ID corresponds to the column model ID in Tables IV and V.

cutoff frequency, while higher BH spin $\chi_{\rm BH}$ induces lower cutoff frequency. These results are consistent with Eq. (21), since larger values of $C_{\rm NS}$ make the tidal disruption of the binary occur at a more inner orbit with a higher orbital frequency, higher values of Q induce weaker tidal force in the vicinity of $R_{\rm ISCO}$, and higher values of $\chi_{\rm BH}$ gives larger spin-orbit repulsion, thus reduces the orbital angular velocity to maintain a circular orbit, decreases the radius of the ISCO, and therefore, makes NS more easily to be disrupted. These parameter dependence of the cutoff frequency shown in Fig. 11 are all consistent with the interpretation based on the comparison between $R_{\rm ISCO}$ and $R_{\rm dis}$ in Eq. (21).

It is also seen that within the numerical accuracy, the normalized cutoff frequency $f_{\rm cut}m_0$ for models with the same values of Q, $\chi_{\rm BH}$, and $C_{\rm NS}$ is approximately identical even though these models have different NS masses, i.e., different EOSs. The relative deviation between $f_{\rm cut}m_0$ within the same group is small, and as a quantity characterizing where tidal disruptions happen, the value of $f_{\rm cut}m_0$ depends solely on the ratio of $R_{\rm dis}$ and $R_{\rm ISCO}$. This dependence of $f_{\rm cut}m_0$ implies the relative location of tidal disruptions depends solely on Q, $\chi_{\rm BH}$, and $C_{\rm NS}$.

C. Massive NS case

Table VI shows the simulation results with a fixed NS mass $M_{\rm NS} = 1.8M_\odot$ but with different EOSs. Massive NSs generally have weak or no tidal disruptions due to their high compactness, as indicated in our analysis in Sec. III A.

To test the validity of fitting formulas derived in previous studies in more compact regions quantitatively, we calculate the χ-square defined as

$$\chi^2 = \frac{1}{N_{\rm model} - N_{\rm para}} \sum_{i=1}^{N_{\rm model}} \Delta_{i,\rm fit}^2, \tag{23}$$

where $N_{\rm model}$ is the number of models in simulations, $\Delta_{i,\rm fit}$ is defined in Eq. (24), and $N_{\rm para}$ is the number of parameters used in the fitting formula.

$\Delta_{\rm fit}$ denotes the ratio of discrepancy of the results between the fitting formulas and the simulation data to the estimated numerical error of the simulation $\Delta_{\rm NR}$, which is defined by

$$\Delta_{\rm fit} = \frac{\hat{M}_{\rm NR} - \hat{M}_{\rm fit}}{\Delta_{\rm NR}}, \tag{24}$$

where $\hat{M}_{\rm NR}$ and $\hat{M}_{\rm fit}$ denote the results from numerical simulations and the prediction of the fitting formulas, respectively, which can be either remnant or ejecta mass. In Refs. [33,46], for ejecta mass, $\Delta_{\rm NR}$ is assumed to be

$$\Delta_{\rm NR} = \sqrt{(\hat{M}_{\rm NR}/10)^2 + (1/50)^2}, \tag{25}$$

which holds for eje_2016 and eje_2020, while for remnant mass, Refs. [38,47] give

$$\Delta_{\rm NR} = \sqrt{(\hat{M}_{\rm NR}/10)^2 + (1/100)^2}, \tag{26}$$

which is the case for rem_2012 and rem_2018.

Since the fitting formulas were derived by minimizing the χ-square in previous simulations, to achieve a benchmark of their accuracy, we first calculate the χ-square of the fitting formulas with $\Delta_{\rm NR}$ from Eq. (25) for the ejecta mass and from Eq. (26) for the remnant mass for numerical-relativity results given in Ref. [32], of which parameters of BH-NS binaries are within the calibrated range. The results are shown in Table VII. These results can be considered as typical values of the χ-square. To evaluate how well the fitting formulas work for our simulations, we compare the χ-square of our simulation data with that of Ref. [32].

Next, we calculate the χ-square for our simulation data with $M_{\rm NS} = 1.8M_\odot$, $C_{\rm NS}$ ranging from 0.194 to 0.252, and C182, C147 models with Eq. (23) and $\Delta_{\rm NR}$ given in Eqs. (25) and (26). For the remnant mass, the χ-squares of M18, C147, and C182 for both fitting formulas are smaller than those of the models in Ref. [32]. For rem_2012, its χ-squares for our simulations are generally smaller than previous simulations and close to unity. $\chi^{2018}_{\rm rem}$ increases as the NS compactness decreases, and is generally larger than the corresponding $\chi^{2012}_{\rm rem}$. As to the ejecta mass, for C182 and C147 models, their χ-squares are smaller than those of models in Ref. [32]. For the M18 case, its $\chi^{2016}_{\rm eje}$ is significantly larger than those of the other three cases, while its $\chi^{2020}_{\rm eje}$ is much smaller. Nevertheless, we find that within the numerical accuracy analyzed in previous

TABLE VII. The χ-squares for different fitting formulas. M18, C182, and C147 denote models with $M_{\rm NS} = 1.8M_\odot$, $C_{\rm NS} = 0.182$, and $C_{\rm NS} = 0.147$, respectively. The first half is χ-square calculated using $\Delta_{\rm NR}$ from Refs. [33,38] to compare with the results in the previous simulations. The second half is χ-square calculated using $\Delta_{\rm NR}$ obtained in our simulations.

	$\chi^{2012}_{\rm rem}$	$\chi^{2018}_{\rm rem}$	$\chi^{2016}_{\rm eje}$	$\chi^{2020}_{\rm eje}$
$\Delta_{\rm NR}$ given in Eqs. (25), (26)				
Models in Ref. [32]	4.75	5.56	0.0250	0.0601
M18	1.35	2.75	0.968	0.00122
C182	0.601	3.38	0.0320	0.0300
C147	1.77	5.47	0.0499	0.0162
$\Delta_{\rm NR}$ given in Eq. (27)				
M18	11.7	28.6	43.0	0.0542
C182	2.53	10.9	1.39	1.31
C147	2.15	6.95	1.20	0.344

studies, their fitting formulas for $\hat{M}_{\rm rem}$ and $\hat{M}_{\rm eje}$ work well even in the compact NS region since the χ-squares are close to unity.

It is not surprised to find that model rem_2012 performs better than model rem_2018 generally in the paper. The simulations used to fit rem_2012 covers a relatively narrow parameter space compared to rem_2018, and around 2/3 of them use $Q = 3$–5 and $\chi^f_{\rm BH} = 0.50$–0.75, consistent with the parameter range in our paper. Therefore, rem_2012 is more likely to behave better when fitting the results from our simulations, while rem_2018 is meant to avoid large errors on a larger scale with the trade-off of lower accuracy in some specific parameter range.

We then calculate the χ-square of fitting formulas using $\Delta_{\rm NR}$ given by our simulations to test whether there could be room for improving the fitting formulas employing higher resolution data of a numerical-relativity simulation. In our research, the numerical error is estimated to be

$$\Delta_{\rm NR} = \sqrt{(\hat{M}_{\rm NR}/10)^2 + (3/1000)^2} \tag{27}$$

(see Appendix A). Equation (27) shows that the numerical errors of our simulations are smaller than those given by Eqs. (25) and (26), and hence, the χ-square calculated based on it gives more severe examination to the fitting formula.

Results are shown in Table VII. The χ-squares for M18 are significantly larger than those of C147 and C182 except for eje_2020, which are much smaller. The reason for this increase is that mergers with compact NSs result in smaller values of $\hat{M}_{\rm rem}$ and $\hat{M}_{\rm eje}$ and therefore sensitive to the lower limit of the estimated numerical error. Assuming a smaller numerical error enhances their χ-squares significantly. $\chi^{2018}_{\rm rem}$ of C182, C147 also increases significantly, while other χ-squares for C147 and C182 models remain close to the unity.

We find that some χ-squares in Table VII are much less than unity. This is because the numerical error we use is the rough upper estimation, which may be overestimated especially when $\hat{M}_{\rm NR}$ is small, and makes χ-squares small.

Therefore, if we assume a smaller numerical error of our simulations, rem_2012, rem_2018, and eje_2016 have room for improvement, particularly for compact NS cases. Their χ-squares increase as the NS compactness increases, and for the M18 case, their χ-squares are significantly larger. This is reasonable because these fitting formulas are calibrated in the parameter space of $C_{\rm NS} < 0.18$. Only $\chi^{2020}_{\rm eje}$ decreases as the compactness increases and has a better performance in the compact NS region. Thus, if we want to estimate the remnant disk mass for $C_{\rm NS} > 0.194$ at higher accuracy, existing fitting formulas require improvement. On the other hand, the fitting formula of the ejecta mass given in Ref. [46] still works well in this region even if we assume a smaller numerical error of our simulations since its χ-square is less than the unity. In addition, if we require a higher accuracy of the estimation of the remnant mass, rem_2012 works better than rem_2018.

IV. CONCLUSION AND DISCUSSION

We perform numerical-relativity simulations for various setups of BH-NS mergers with $Q = 3, 5$, $\chi_{\rm BH} = 0.5, 0.75$, and $C_{\rm NS} = 0.147 - 0.252$ varying the NS mass. Our results with the fixed NS compactness $C_{\rm NS} = 0.182$ and 0.147 show that given the identical values of Q, $\chi_{\rm BH}$, and $C_{\rm NS}$, $\hat{M}_{\rm rem}$ and $f_{\rm cut} m_0$ agree with each other within the numerical accuracy of our study. We also found that this is the case for $\hat{M}_{\rm eje}$, except for only one dataset which is slightly out of the numerical accuracy. Therefore, the hypothesis that $\hat{M}_{\rm rem}$, $\hat{M}_{\rm eje}$, $v_{\rm eje}$ and $f_{\rm cut} m_0$ depend only on Q, $\chi_{\rm BH}$, and $C_{\rm NS}$ is approximately true for the NS mass in a wide range of $1.1 - 1.7M_\odot$. This justifies the approach of studying the dependence of NS tidal disruptions on the NS compactness by fixing the NS mass but changing the EOS, which is employed in the previous studies.

We then performed numerical-relativity simulations of BH-NS mergers for a large value of the NS mass ($M_{\rm NS} = 1.8M_\odot$), and examined the accuracy of the previous fitting formulas of $\hat{M}_{\rm rem}$, $\hat{M}_{\rm eje}$, and ejecta velocity $v_{\rm eje}$ for the system with a large value of the NS compactness ($C_{\rm NS} \geq 0.19$). As to the four fitting formulas of $\hat{M}_{\rm rem}$ and $\hat{M}_{\rm eje}$, we find that they still work well for compact NSs within the error range of their studies. However, if we require a higher-precision prediction, the fitting formulas of the remnant mass could give inaccurate predictions for $C_{\rm NS} > 0.194$ cases, leaving room for further improvements, and rem_2012 is generally more accurate than rem_2018. As to the ejecta mass, the fitting formula

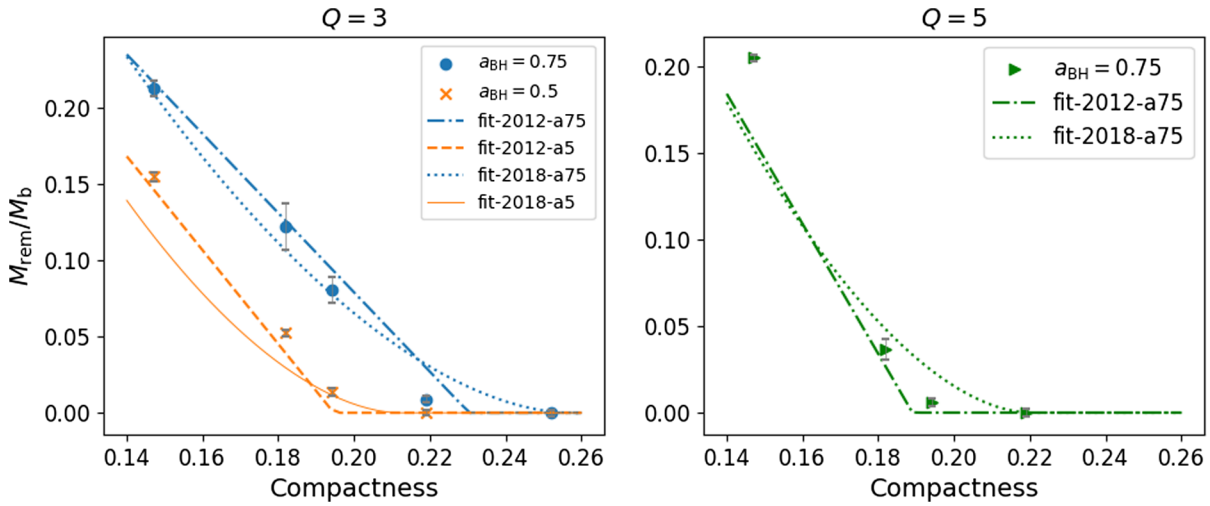

FIG. 12. Normalized remnant mass as a function of the compactness. For models with the same values of Q, χ_{BH}, and C_{NS}, since the discrepancies between them are within the margin of error, the simulation results are taken randomly from one of them, and the error bar is taken to be the largest error range of them.

eje_2020 from Ref. [46] still works well for more massive NSs with C_{NS} between 0.194 and 0.252.

For the case of ejecta velocity, we corrected the data of average ejecta velocity in Ref. [33] to take into account the gravitational potential effect, and recalibrated the ejecta-velocity fitting formula employing these corrected data as well as the results obtained in our present simulations. We obtained the simple linear function as the fitting formula between v_{eje} and Q as in Ref. [33]. We found that the predicted ejecta velocity is systematically smaller than those of the previous studies. The relative fitting error of the fitting formula is around 10% for the data in this paper and in Ref. [33], and grows to 18% if we use all the data to obtain a new fitting formula. It is larger than 10% of the relative numerical error of v_{eje} estimated from different resolutions runs. This indicates that the ejecta velocity has a dependence on the other parameters which cannot be captured by the simple linear relations between v_{eje} and Q.

Our results give some guidance on how to improve the fitting formulas for the remnant mass. From Fig. 12, which shows $\hat{M}_{rem}$ as a function of C_{NS}, we can see that rem_2012 works best for Q3a5 models, even for compact NSs. The inaccuracy of the fitting formula is caused mainly by the large discrepancies between the fitting and the simulation results for Q3a75 models. The fitting formula generally overestimates the remnant mass for all Q3a75 models, but this overestimation is only significant for mergers with small remnant masses, i.e., with compact NSs. For example, H-Q3a75 has only 0.9% of its baryon mass remaining outside the BH after the merger, and the rem_2012 gives a prediction of 2.8%. Rem_2018 overestimates the remnant mass for compact NSs and is generally less accurate than rem_2012. Therefore, a linear function of C_{NS} is still a good choice for the fitting formula of the remnant mass and the second term in Eq. (11) requires modification to get more accurate results.

The improvement in the fitting formulas in such a parameter region may be not very important at this moment, since the overestimation is only significant for the cases having weak tidal disruptions, for which only faint EM counterparts can associate with the GW signals and are less likely to be detected by observations. However, the improvement in such a parameter region can play an important role in interpreting the observational data once faint EM counterparts are detected or deep EM upper-limits are obtained in the future BH-NS GW events (cf, GW190425 and GW190814 [101,102]).

ACKNOWLEDGMENTS

We would like to thank Francois Foucart for his helpful comments. Numerical computation was performed on Yukawa21 at Yukawa Institute for Theoretical Physics, Kyoto University and the Yamazaki, Sakura, Cobra, and Raven clusters at Max Planck Computing and Data Facility. This work was supported by Grant-in-Aid for Scientific Research (20H00158, 23H04900, and 23H01172) of JSPS/MEXT. Shichuan Chen is supported by China Scholarship Council.

APPENDIX A: ESTIMATION OF ERROR CAUSED BY GRID RESOLUTION

The mass of the remnant disk and the ejecta are only a fraction of the NS mass, and thus, can have large errors in the numerical results. Here we estimate the errors due to finite grid resolutions, as shown in Fig. 13. Both masses depend sensitively on the grid resolution.

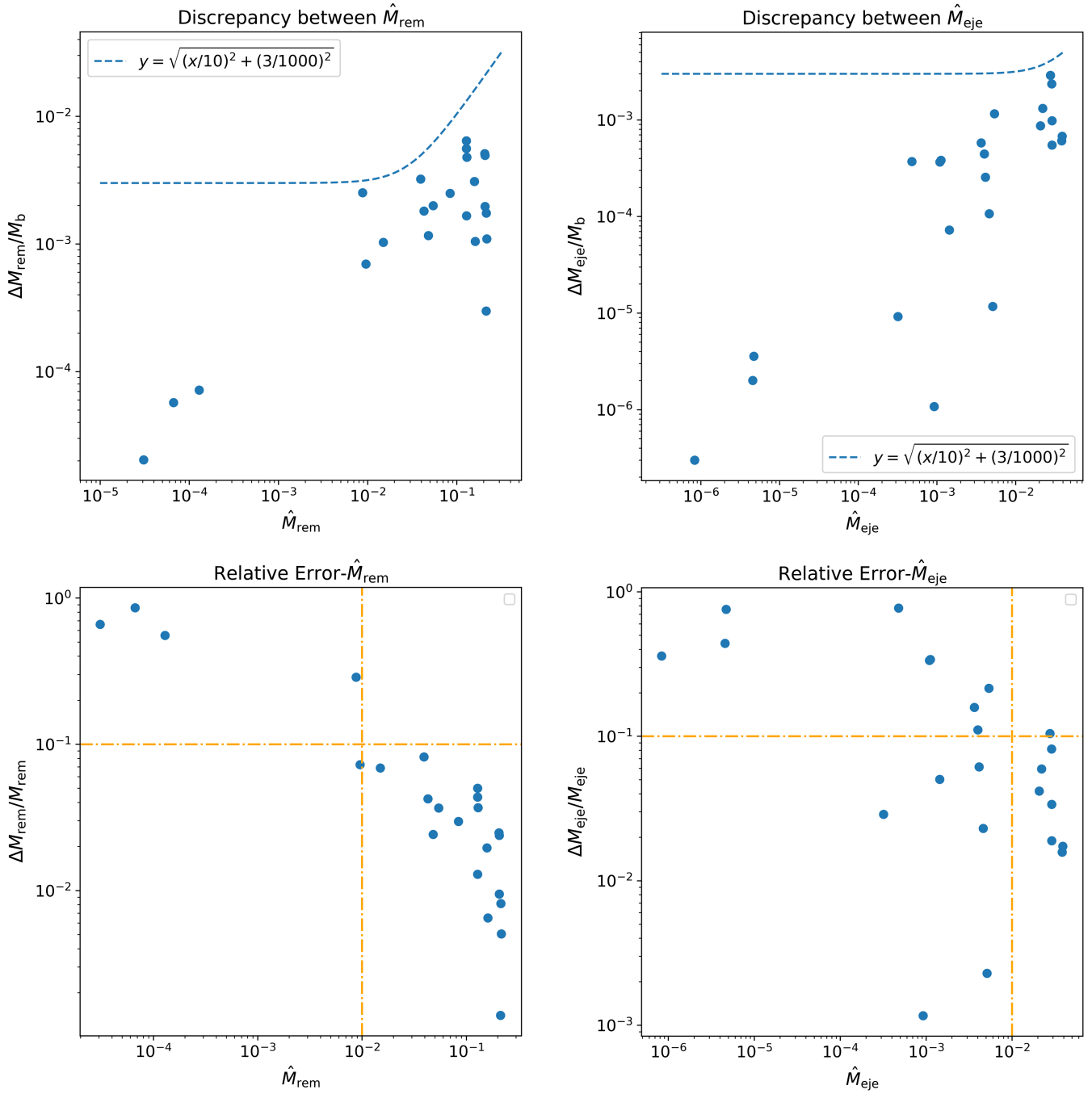

FIG. 13. Discrepancy of $M_{\rm rem}/M_{\rm b}$ and $M_{\rm eje}/M_{\rm b}$ between runs with different grid resolutions. The x-axis is taken to the results from $N=82$ runs. The scatters are taken to be the minimum discrepancy among N62, N82, and N102 runs. The blue dashed curves are an upper estimation of the numerical error of the normalized remnant and ejecta mass, and the orange dashed lines are an estimation of the relative numerical error.

As shown in the lower plots, for $\hat{M}>0.01M_{\odot}$, the relative errors are generally less than 10%, while for very small values of $\hat{M}$, the relative error can be up to 100%. We expect that it is possible to obtain a function for the numerical errors, analogous to that given in Eq. (25) and Eq. (26). Therefore, the coefficient in front of $\hat{M}$ in Eq. (27) can be taken as 0.1, and the constant part is taken as 0.003. As shown in Fig. 13, the error for $\hat{M}_{\rm eje}$ and $\hat{M}_{\rm rem}$ can be described using a uniform estimation as it is in Eq. (27).

We list numerical results for some models with different grid resolutions $N=62$, 82 and 102 in Table VIII. The relative error between N82 and N102 runs ranges from 0.9% to 3% for $\hat{M}_{\rm rem}$, and ranges from 1% to 34% for $\hat{M}_{\rm eje}$. The relative error of the ejecta velocity between $N=82$

TABLE VIII. Several numerical results for models 15H-Q3a75M18, H-Q3a75M1220, HB-Q3a75M1428, and HB-Q5a75M1428 with different grid resolutions $N = 62$, 82, and 102. All the quantities are defined in the body text.

N	$\hat{M}_{\rm rem}$	$\hat{M}_{\rm eje}$	$v_{\rm eje}$	$f_{\rm cut} m_0$	$\chi_{\rm BH}$
	15H-Q3a75M18				
62	0.0840	0.00144	0.155	0.0762	0.870
82	0.0807	0.00151	0.159	0.0849	0.870
102	0.0782	0.00203	0.172	0.0883	0.870
	H-Q3a75M1220				
62	0.213	0.0290	0.181	0.0384	0.863
82	0.212	0.0296	0.185	0.0394	0.871
102	0.210	0.0303	0.188	0.0398	0.868
	HB-Q3a75M1428				
62	0.128	0.00513	0.172	0.0666	0.873
82	0.124	0.00589	0.182	0.0687	0.870
102	0.122	0.005884	0.185	0.0701	0.870
	HB-Q5a75M1428				
62	0.0393	0.000414	0.200	0.0993	0.845
82	0.0360	0.00542	0.191	0.1014	0.845
102	0.0327	0.00527	0.192	0.1016	0.845
	15H-Q5a75M1691				
62	0.0428	0.000463	0.177	0.0993	0.845
82	0.0369	0.00474	0.187	0.1011	0.845
102	0.0351	0.00491	0.185	0.1016	0.845

and $N = 62$ runs ranges from 2% to 5%. The discrepancies of $f_{\rm cut} m_0$ between $N = 62$ and $N = 82$ range from 0.4% to 5%. The discrepancies of the spin are around 0.1% for the three resolutions. In general, due to the complexity of hydrodynamics, hydrodynamic quantities have larger uncertainties. $\hat{M}_{\rm rem}$ decreases as the grid resolution increases, while systematic convergence properties of other quantities are not seen, and the discrepancies of numerical results among different resolutions do not decrease necessarily as the grid resolution increases. The reason for this unsystematic behavior is likely that (i) in the presence of shocks (e.g., in the tidal tail), numerical accuracy becomes the first-order convergence and hence the error can be enhanced in an unpredicted manner. (ii) the motion of the matters is affected by the background atmosphere in the simulations [32], the error associated with the artificial atmosphere decreases significantly as grid resolutions are improved, due to the suppression of spurious shocks at the stellar surface.

APPENDIX B: CORRECTION OF EJECTA VELOCITY

Different from Eq. (4), the kinetic energy of the ejecta defined in Ref. [33] is

$$T_{\rm eje,old} := E_{\rm eje} - U_{\rm eje} - M_{\rm eje}. \tag{B1}$$

The total energy of the ejecta $E_{\rm eje}$ is defined by

$$E_{\rm eje} := \int_{-u_t>1, r>r_{\rm AH}} \rho_* \hat{e} d^3x. \tag{B2}$$

The internal energy of the ejecta $U_{\rm eje}$ is defined by

$$U_{\rm eje} := \int_{-u_t>1, r>r_{\rm AH}} \rho_* \epsilon d^3x. \tag{B3}$$

The mass of ejecta $M_{\rm eje}$ is defined as in Eq. (3). The definitions of ρ_*, $\hat{e}$, and ϵ are listed in Table I.

Assuming the Newtonian dynamics, the averaged velocity of the ejecta can be evaluated as

$$v_{\rm eje,old} := \sqrt{\frac{2T_{\rm eje,old}}{M_{\rm eje}}}. \tag{B4}$$

The gravitational potential energy is not excluded in $T_{\rm eje,old}$, and $v_{\rm eje,old}$ is overestimated. To subtract the effect of this gravitational potential energy, we can approximately correct the velocity as in Ref. [34]

$$v_{\rm eje,cor} := \sqrt{v_{\rm eje,old}^2 - \frac{2m_0}{v_{\rm eje,old}(t - t_{\rm merger})}}, \tag{B5}$$

where $v_{\rm eje,old}$ is evaluated at time t.

Figure 14 shows the time evolution of $v_{\rm eje}$ with different definitions for a representative model 15H-Q3a75M1691. If we choose $v_{\rm eje}$ defined in Eq. (5) to be the fiducial value, we find that $v_{\rm eje,old}$ is still overestimated by ∼50% at 12 ms after the onset of the merger. The corrected velocity of ejecta $v_{\rm eje,cor}$ is closer to $v_{\rm eje}$ compared to $v_{\rm eje,old}$, and asymptotically approaches $v_{\rm eje}$ at 10 ms after the onset of the merger. Thus, it is reasonable to use Eq. (B5) to correct previous data of the average velocity of ejecta.

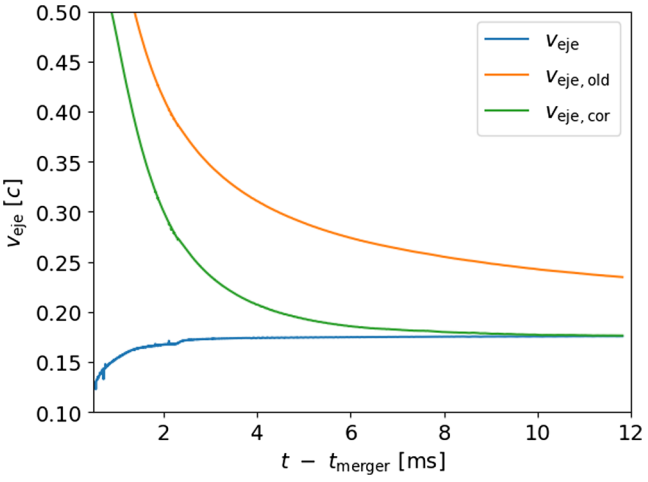

FIG. 14. Time evolution of $v_{\rm eje}$ for model 15H-Q3a75M1691 with different definitions. Here, the results are from $N = 82$ runs. $v_{\rm eje}$ is defined by Eq. (20), $v_{\rm eje,old}$ by Eq. (B4), and $v_{\rm eje,cor}$ by Eq. (B5).

[1] B. P. Abbott *et al.* (LIGO Scientific Collaboration and Virgo Collaboration), Phys. Rev. Lett. **116**, 061102 (2016).
[2] B. P. Abbott *et al.* (LIGO Scientific Collaboration and Virgo Collaboration), Phys. Rev. Lett. **119**, 161101 (2017).
[3] B. P. Abbott *et al.*, Astrophys. J. **848**, L12 (2017).
[4] B. P. Abbott *et al.*, Astrophys. J. **848**, L13 (2017).
[5] A. Goldstein *et al.*, Astrophys. J. Lett. **848**, L14 (2017).
[6] LIGO Scientific Collaboration and Virgo Collaboration, GRB Coordinates Network **21505**, 1 (2017), https://ui.adsabs.harvard.edu/abs/2017GCN.21505....1L/abstract.
[7] S. De, D. Finstad, J. M. Lattimer, D. A. Brown, E. Berger, and C. M. Biwer, Phys. Rev. Lett. **121**, 091102 (2018).
[8] B. P. Abbott *et al.* (The LIGO Scientific Collaboration and the Virgo Collaboration), Phys. Rev. Lett. **121**, 161101 (2018).
[9] B. P. Abbott *et al.* (LIGO Scientific Collaboration and Virgo Collaboration), Phys. Rev. X **9**, 011001 (2019).
[10] T. Narikawa, N. Uchikata, K. Kawaguchi, K. Kiuchi, K. Kyutoku, M. Shibata, and H. Tagoshi, Phys. Rev. Res. **2**, 043039 (2020).
[11] V. Savchenko *et al.*, Astrophys. J. Lett. **848**, L15 (2017).
[12] M. Tanaka, K. Hotokezaka, K. Kyutoku, S. Wanajo, K. Kiuchi, Y. Sekiguchi, and M. Shibata, Astrophys. J. **780**, 31 (2013).
[13] J. M. Lattimer and D. N. Schramm, Astrophys. J. Lett. **192**, L145 (1974).
[14] D. Eichler, M. Livio, T. Piran, and D. N. Schramm, Nature (London) **340**, 126 (1989).
[15] C. Freiburghaus, S. Rosswog, and F.-K. Thielemann, Astrophys. J. **525**, L121 (1999).
[16] M. R. Drout *et al.*, Science **358**, 1570 (2017).
[17] E. Pian, P. D'Avanzo, S. Benetti, M. Branchesi, E. Brocato, S. Campana, E. Cappellaro, V. D'Elia, J. Fynbo, F. Getman, G. Ghirlanda, G. Ghisellini, A. Grado, G. Greco, J. Hjorth, C. Kouveliotou, A. Levan, L. Limatola, and D. Vergani, Nature (London) **551**, 67 (2017).
[18] R. Abbott *et al.*, Astrophys. J. **915**, L5 (2021).
[19] B. P. Abbott *et al.*, Astrophys. J. Lett. **892**, L3 (2020).
[20] K. Kyutoku, S. Fujibayashi, K. Hayashi, K. Kawaguchi, K. Kiuchi, M. Shibata, and M. Tanaka, Astrophys. J. **890**, L4 (2020).
[21] M. Shibata and K. Taniguchi, Living Rev. Relativity **14**, 6 (2011).
[22] M. Shibata and K. Uryū, Phys. Rev. D **74**, 121503 (2006).
[23] M. Shibata and K. Uryū, Classical Quantum Gravity **24**, S125 (2007).
[24] M. Shibata and K. Taniguchi, Phys. Rev. D **77**, 084015 (2008).
[25] Z. B. Etienne, J. A. Faber, Y. T. Liu, S. L. Shapiro, K. Taniguchi, and T. W. Baumgarte, Phys. Rev. D **77**, 084002 (2008).
[26] M. D. Duez, F. Foucart, L. E. Kidder, H. P. Pfeiffer, M. A. Scheel, and S. A. Teukolsky, Phys. Rev. D **78**, 104015 (2008).
[27] T. Yamamoto, M. Shibata, and K. Taniguchi, Phys. Rev. D **78**, 064054 (2008).
[28] Z. B. Etienne, Y. T. Liu, S. L. Shapiro, and T. W. Baumgarte, Phys. Rev. D **79**, 044024 (2009).
[29] M. Shibata, K. Kyutoku, T. Yamamoto, and K. Taniguchi, Phys. Rev. D **79**, 044030 (2009).
[30] F. Foucart, M. D. Duez, L. E. Kidder, and S. A. Teukolsky, Phys. Rev. D **83**, 024005 (2011).
[31] K. Kyutoku, M. Shibata, and K. Taniguchi, Phys. Rev. D **82**, 044049 (2010).
[32] K. Kyutoku, K. Ioka, H. Okawa, M. Shibata, and K. Taniguchi, Phys. Rev. D **92**, 044028 (2015).
[33] K. Kawaguchi, K. Kyutoku, M. Shibata, and M. Tanaka, Astrophys. J. **825**, 52 (2016).
[34] K. Hayashi, K. Kawaguchi, K. Kiuchi, K. Kyutoku, and M. Shibata, Phys. Rev. D **103**, 043007 (2021).
[35] F. Foucart, M. D. Duez, L. E. Kidder, S. M. Nissanke, H. P. Pfeiffer, and M. A. Scheel, Phys. Rev. D **99**, 103025 (2019).
[36] W. Brege, M. D. Duez, F. Foucart, M. B. Deaton, J. Caro, D. A. Hemberger, L. E. Kidder, E. O'Connor, H. P. Pfeiffer, and M. A. Scheel, Phys. Rev. D **98**, 063009 (2018).
[37] F. Foucart, M. B. Deaton, M. D. Duez, L. E. Kidder, I. MacDonald, C. D. Ott, H. P. Pfeiffer, M. A. Scheel, B. Szilagyi, and S. A. Teukolsky, Phys. Rev. D **87**, 084006 (2013).
[38] F. Foucart, Phys. Rev. D **86**, 124007 (2012).
[39] F. Foucart, M. D. Duez, L. E. Kidder, M. A. Scheel, B. Szilagyi, and S. A. Teukolsky, Phys. Rev. D **85**, 044015 (2012).
[40] G. Lovelace, M. D. Duez, F. Foucart, L. E. Kidder, H. P. Pfeiffer, M. A. Scheel, and B. Szilágyi, Classical Quantum Gravity **30**, 135004 (2013).
[41] F. Foucart, M. B. Deaton, M. D. Duez, E. O'Connor, C. D. Ott, R. Haas, L. E. Kidder, H. P. Pfeiffer, M. A. Scheel, and B. Szilagyi, Phys. Rev. D **90**, 024026 (2014).
[42] K. Kawaguchi, K. Kyutoku, H. Nakano, H. Okawa, M. Shibata, and K. Taniguchi, Phys. Rev. D **92**, 024014 (2015).
[43] K. Kyutoku, M. Shibata, and K. Taniguchi, Living Rev. Relativity **24**, 5 (2021).
[44] V. Ferrari, L. Gualtieri, and F. Pannarale, Phys. Rev. D **81**, 064026 (2010).
[45] K. Kyutoku, H. Okawa, M. Shibata, and K. Taniguchi, Phys. Rev. D **84**, 064018 (2011).
[46] C. J. Krüger and F. Foucart, Phys. Rev. D **101**, 103002 (2020).
[47] F. Foucart, T. Hinderer, and S. Nissanke, Phys. Rev. D **98**, 081501 (2018).
[48] F. Pannarale and F. Ohme, Astrophys. J. Lett. **791**, L7 (2014).
[49] D. Radice, A. Perego, F. Zappa, and S. Bernuzzi, Astrophys. J. Lett. **852**, L29 (2018).
[50] T. Hinderer, S. Nissanke, F. Foucart, K. Hotokezaka, T. Vincent, M. Kasliwal, P. Schmidt, A. R. Williamson, D. A. Nichols, M. D. Duez, L. E. Kidder, H. P. Pfeiffer, and M. A. Scheel, Phys. Rev. D **100**, 063021 (2019).
[51] M. W. Coughlin, T. Dietrich, B. Margalit, and B. D. Metzger, Mon. Not. R. Astron. Soc. **489**, L91 (2019).
[52] C. Barbieri, O. S. Salafia, M. Colpi, G. Ghirlanda, A. Perego, and A. Colombo, Astrophys. J. Lett. **887**, L35 (2019).
[53] I. Andreoni *et al.*, Astrophys. J. **890**, 131 (2020).
[54] S. Ascenzi, N. D. Lillo, C.-J. Haster, F. Ohme, and F. Pannarale, Astrophys. J. **877**, 94 (2019).

[55] T. M. Tauris, M. Kramer, P. C. C. Freire, N. Wex, H.-T. Janka, N. Langer, P. Podsiadlowski, E. Bozzo, S. Chaty, M. U. Kruckow, E. P. J. van den Heuvel, J. Antoniadis, R. P. Breton, and D. J. Champion, Astrophys. J. **846**, 170 (2017).
[56] N. Farrow, X.-J. Zhu, and E. Thrane, Astrophys. J. **876**, 18 (2019).
[57] P. B. Demorest, T. Pennucci, S. M. Ransom, M. S. E. Roberts, and J. W. T. Hessels, Nature (London) **467**, 1081 (2010).
[58] J. Antoniadis *et al.*, Science **340**, 1233232 (2013).
[59] R. Abbott *et al.*, Astrophys. J. **896**, L44 (2020).
[60] K. Kiuchi, K. Kawaguchi, K. Kyutoku, Y. Sekiguchi, M. Shibata, and K. Taniguchi, Phys. Rev. D **96**, 084060 (2017).
[61] M. Campanelli, C. O. Lousto, P. Marronetti, and Y. Zlochower, Phys. Rev. Lett. **96**, 111101 (2006).
[62] J. G. Baker, J. Centrella, D.-I. Choi, M. Koppitz, and J. van Meter, Phys. Rev. Lett. **96**, 111102 (2006).
[63] P. Marronetti, W. Tichy, B. Brügmann, J. González, and U. Sperhake, Phys. Rev. D **77**, 064010 (2008).
[64] M. Shibata and T. Nakamura, Phys. Rev. D **52**, 5428 (1995).
[65] T. W. Baumgarte and S. L. Shapiro, Phys. Rev. D **59**, 024007 (1998).
[66] D. Hilditch, S. Bernuzzi, M. Thierfelder, Z. Cao, W. Tichy, and B. Brügmann, Phys. Rev. D **88**, 084057 (2013).
[67] A. Mignone and G. Bodo, Mon. Not. R. Astron. Soc. **364**, 126 (2005).
[68] C. J. White, J. M. Stone, and C. F. Gammie, Astrophys. J. Suppl. Ser. **225**, 22 (2016).
[69] K. Kiuchi, L. E. Held, Y. Sekiguchi, and M. Shibata, Phys. Rev. D **106**, 124041 (2022).
[70] L. J. Papenfort, S. D. Tootle, P. Grandclément, E. R. Most, and L. Rezzolla, Phys. Rev. D **104**, 024057 (2021).
[71] J. M. Lattimer and M. Prakash, Science **304**, 536 (2004).
[72] J. S. Read, B. D. Lackey, B. J. Owen, and J. L. Friedman, Phys. Rev. D **79**, 124032 (2009).
[73] J. S. Read, C. Markakis, M. Shibata, K. Uryū, J. D. E. Creighton, and J. L. Friedman, Phys. Rev. D **79**, 124033 (2009).
[74] B. D. Lackey, K. Kyutoku, M. Shibata, P. R. Brady, and J. L. Friedman, Phys. Rev. D **85**, 044061 (2012).
[75] K. Hotokezaka, K. Kiuchi, K. Kyutoku, H. Okawa, Y.-i. Sekiguchi, M. Shibata, and K. Taniguchi, Phys. Rev. D **87**, 024001 (2013).
[76] C. O. Lousto, H. Nakano, Y. Zlochower, and M. Campanelli, Phys. Rev. D **82**, 104057 (2010).
[77] C. Reisswig and D. Pollney, Classical Quantum Gravity **28**, 195015 (2011).
[78] J. M. Bardeen, W. H. Press, and S. A. Teukolsky, Astrophys. J. **178**, 347 (1972).
[79] A. Akmal, V. R. Pandharipande, and D. G. Ravenhall, Phys. Rev. C **58**, 1804 (1998).
[80] N. K. Glendenning and S. A. Moszkowski, Phys. Rev. Lett. **67**, 2414 (1991).
[81] B. D. Lackey, M. Nayyar, and B. J. Owen, Phys. Rev. D **73**, 024021 (2006).
[82] T. Hinderer, S. Nissanke, F. Foucart, K. Hotokezaka, T. Vincent, M. Kasliwal, P. Schmidt, A. R. Williamson, D. A. Nichols, M. D. Duez, L. E. Kidder, H. P. Pfeiffer, and M. A. Scheel, Phys. Rev. D **100**, 063021 (2019).
[83] S. Chawla, M. Anderson, M. Besselman, L. Lehner, S. L. Liebling, P. M. Motl, and D. Neilsen, Phys. Rev. Lett. **105**, 111101 (2010).
[84] M. D. Duez, F. Foucart, L. E. Kidder, C. D. Ott, and S. A. Teukolsky, Classical Quantum Gravity **27**, 114106 (2010).
[85] Z. B. Etienne, Y. T. Liu, V. Paschalidis, and S. L. Shapiro, Phys. Rev. D **85**, 064029 (2012).
[86] Z. B. Etienne, V. Paschalidis, and S. L. Shapiro, Phys. Rev. D **86**, 084026 (2012).
[87] M. B. Deaton, M. D. Duez, F. Foucart, E. O'Connor, C. D. Ott, L. E. Kidder, C. D. Muhlberger, M. A. Scheel, and B. Szilagyi, Astrophys. J. **776**, 47 (2013).
[88] V. Paschalidis, M. Ruiz, and S. L. Shapiro, Astrophys. J. **806**, L14 (2015).
[89] F. Foucart, D. Desai, W. Brege, M. D. Duez, D. Kasen, D. A. Hemberger, L. E. Kidder, H. P. Pfeiffer, and M. A. Scheel, Classical Quantum Gravity **34**, 044002 (2017).
[90] K. Kyutoku, K. Kiuchi, Y. Sekiguchi, M. Shibata, and K. Taniguchi, Phys. Rev. D **97**, 023009 (2018).
[91] M. Ruiz, S. L. Shapiro, and A. Tsokaros, Phys. Rev. D **98**, 123017 (2018).
[92] F. Foucart, M. D. Duez, T. Hinderer, J. Caro, A. R. Williamson, M. Boyle, A. Buonanno, R. Haas, D. A. Hemberger, L. E. Kidder, H. P. Pfeiffer, and M. A. Scheel, Phys. Rev. D **99**, 044008 (2019).
[93] J. M. Lattimer and M. Prakash, Astrophys. J. **550**, 426 (2001).
[94] M. Vallisneri, Phys. Rev. Lett. **84**, 3519 (2000).
[95] F. Pannarale, E. Berti, K. Kyutoku, B. D. Lackey, and M. Shibata, Phys. Rev. D **92**, 081504 (2015).
[96] F. Foucart, L. Buchman, M. D. Duez, M. Grudich, L. E. Kidder, I. MacDonald, A. Mroue, H. P. Pfeiffer, M. A. Scheel, and B. Szilagyi, Phys. Rev. D **88**, 064017 (2013).
[97] T. Nakamura and M. Sasaki, Phys. Lett. **106B**, 69 (1981).
[98] S. L. Shapiro and I. M. Wasserman, Astrophys. J. **260**, 838 (1982).
[99] T. Nakamura and K. Ichi Oohara, Phys. Lett. **98A**, 403 (1983).
[100] M. Shibata, *Numerical Relativity* (World Scientific, Singapore, 2015), Vol. 1.
[101] K. Kyutoku, S. Fujibayashi, K. Hayashi, K. Kawaguchi, K. Kiuchi, M. Shibata, and M. Tanaka, Astrophys. J. Lett. **890**, L4 (2020).
[102] K. Kawaguchi, M. Shibata, and M. Tanaka, Astrophys. J. **893**, 153 (2020).